

Uniform Metallicity Measurements of M Dwarf Planet Hosts Support Metallicity-Dependent Sub-Neptune Formation

EMMA V. TURTELBOOM ^{1,2,*} STEVEN GIACALONE ^{3,†} REBECCA GORE ⁴ COURTNEY D. DRESSING ²
RYAN CLOUTIER ¹ KARINA KIMANI-STEWART ^{5,6} AIDA BEHMARD ⁷ C.M. LISSE ⁸ AND M.L. SITKO ⁹

¹*Department of Physics & Astronomy, McMaster University, 1280 Main Street West, Hamilton, Ontario, Canada*

²*Department of Astronomy, 501 Campbell Hall, University of California, Berkeley, CA 94720, USA*

³*Department of Astronomy, California Institute of Technology, Pasadena, CA 91125, USA*

⁴*Department of Physics & Astronomy, San Francisco State University, 1600 Holloway Avenue, San Francisco, CA 94132, USA*

⁵*Department of Physics & Astronomy, Georgia State University, 25 Park Place, Atlanta, GA 30303, USA*

⁶*RECONS Institute, Chambersburg, PA 17201, USA*

⁷*Center for Computational Astrophysics, Flatiron Institute, 162 Fifth Ave, New York, NY 10010, USA*

⁸*Johns Hopkins University Applied Physics Laboratory, 11100 Johns Hopkins Road, Laurel, MD 20723, USA*

⁹*Center for Exoplanetary Systems, Space Science Institute, 4750 Walnut Street, Suite 205, Boulder, CO 80301, USA*

ABSTRACT

M dwarfs are the most common sites of planet formation in the Milky Way. Planet occurrence and composition are closely linked with the availability of metals in protoplanetary disks, which can be probed by measuring the metallicity of planet host stars. In this work, we measure the metallicities ($[M/H]$ and $[Fe/H]$) of 59 M dwarfs hosting 76 planets and candidates using medium-resolution near-infrared spectra collected with IRTF/SpeX. We combine these results with literature metallicity measurements for planet-hosting cool dwarfs, and present a sample of 86 stars hosting 142 candidate, validated, and confirmed planets with homogeneously derived stellar parameters. Using our updated stellar radii, we calculate planet radii from TESS transit depths for both the confirmed ($N = 51$, $0.6 - 12.5 R_{\oplus}$, median $R_p = 1.8R_{\oplus}$) and candidate ($N = 25$, $0.6 - 7.2 R_{\oplus}$, median $R_p = 2.1R_{\oplus}$) planets. We compare the metallicity distributions of super-Earth and sub-Neptune host stars, finding that M dwarfs hosting sub-Neptunes are statistically more metal-rich than those hosting super-Earths. This result is robust to the radius valley prescription used, and is likely not due to differences in the stellar samples considered. This result supports the hypothesized formation pathway whereby sub-Neptunes form beyond the water ice line where they can accrete volatiles before migrating inwards to their observed locations. The enhanced inventories of refractory elements throughout the disk and of volatiles beyond the ice line in metal-rich disks around low-mass stars may contribute to the preference seen in the observed planet sample for sub-Neptunes to orbit metal-rich M dwarfs.

1. INTRODUCTION

Our understanding of the more than 6000 exoplanets discovered to date is highly dependent on our understanding of the stars that they orbit. Despite the growing sample of directly imaged planets around young stars (e.g. Lagrange et al. 2009; Macintosh et al. 2015), the majority of exoplanets orbit older stars and are discovered using transit and radial velocity (RV) observations.

These indirect detection methods infer the presence and parameters of a planet through changes in host star observables. As a result, imprecise or inaccurate stellar mass, radius, effective temperature, surface gravity, and metallicity values lead to inaccurate planet parameters and incorrect inferences about planetary system formation. Previous work (e.g. Petigura 2020; MacDougall et al. 2023) has demonstrated that reducing uncertainties in stellar parameters reveal planet demographic features in sharper detail, enabling more precise connections between observed planets and planet formation mechanisms.

Metallicity and mass are two fundamental characteristics of stars that impact planet formation, as they re-

Corresponding author: Emma V. Turtelboom
eturtelboom@berkeley.edu

* William & Caroline Herschel Postdoctoral Fellow

† NSF Astronomy and Astrophysics Postdoctoral Fellow

flect the total mass, lifetime, and metallicity of the disks in which planets form (Williams & Cieza 2011; Ribas et al. 2015). The metal content of these disks sets the solid material available to form protoplanet cores, and thus stellar metallicities are commonly used as a proxy for disk dust-to-gas ratios. Small planets ($< 4R_{\oplus}$) are more common around low-mass stars than around Sun-like stars (Dressing & Charbonneau 2013; Hardegree-Ullman et al. 2019; Ment & Charbonneau 2023; Gillis et al. 2026). On the other hand, the occurrence of short-period ($P < 10$ d) giant planets, known as Hot Jupiters, appears to peak around solar-mass stars (Beleznay & Kunimoto 2022; Bryant et al. 2023). The occurrence of giant planets is highly correlated with stellar metallicity (Santos et al. 2001; Fischer & Valenti 2005; Ghezzi et al. 2018). A metal-rich disk increases the chance that a protoplanet reaches the critical mass to trigger runaway gas accretion before the gas disk dissipates, resulting in a strong occurrence-metallicity relationship for gas giants.

On the other hand, the relationship between small planet occurrence and stellar metallicity is much more uncertain. Buchhave et al. (2012) and Kutra et al. (2021) found that the formation of small planets may be agnostic to stellar metallicity, while Lu et al. (2020) report an increase in planet occurrence for planets with radii between 2 and 5 R_{\oplus} as stellar metallicity increases. Small extrasolar planets, with radii between that of the Earth and of Neptune, are not found in the Solar System, but are very common in the Milky Way (Howard et al. 2012). Furthermore, the occurrence of small planets increases around low-mass stars, which are themselves the most common stars in the Milky Way (Henry & Jao 2024). Therefore, understanding how small planets around low-mass stars form and evolve is critical to forming a full picture of planet formation in the solar neighbourhood and beyond.

With the large sample of observed planets, it is possible to compare and characterize planet sub-populations. For example, small planets can be further divided into super-Earths ($R_p \lesssim 1.8R_{\oplus}$) and sub-Neptunes ($2R_{\oplus} \lesssim R_p \lesssim 4R_{\oplus}$). These two groups are separated by the radius valley, first posited to exist following theoretical arguments (Owen & Wu 2013) and later observed in radial velocity survey results (Fulton et al. 2017). The dominant physical processes governing the radius valley remain unclear. Super-Earths and sub-Neptunes may form as distinct populations (e.g. Lee et al. 2022; Lopez & Rice 2018; Chiang & Laughlin 2013; Dawson et al. 2015; MacDonald et al. 2020), may be only distinguished by post-formation atmospheric mass-loss (e.g.

Bean et al. 2021), or may be formed through a combination of these two scenarios (Burn et al. 2024).

Constraining planet interiors to reveal the nature of the radius valley is challenging due to degeneracies inherent in inferring complex interior structures from few observables: planet mass, radius, and instellation. In one scenario, sub-Neptunes are enriched in volatiles (e.g. Léger et al. 2004; Rogers 2015; Mousis et al. 2020; Burn et al. 2024) while super-Earths are dry and rocky (e.g. Rogers et al. 2025). Alternatively, sub-Neptunes may include carbon-rich planets (Lin & Seager 2025), ice-rock mixtures (Kovačević et al. 2022), and volatile-poor planets (Chen et al. 2025). If super-Earths and sub-Neptunes form in different disk locations, these environmental differences may also be evident in their host stars (Brugger et al. 2017; Owen & Murray-Clay 2018a). Characterizing planet host stars therefore offers another window into the physical properties underlying the observed radius valley.

Previous investigations of the radius valley around low-mass stars found that as stellar mass decreases super-Earths become an order of magnitude more common than sub-Neptunes Ment & Charbonneau (2023); Gillis et al. (2026). Furthermore, the slope of radius valley separating the two populations decreases in magnitude in period-radius space (Gupta et al. 2022) and the radius valley moves to higher planet instellation (Parashivamurthy & Mulders 2025; Gillis et al. 2026) with decreasing stellar mass. There remain, however, clear sub-populations in density space (Luque & Pallé 2022), suggesting that compositionally distinct super-Earths and sub-Neptunes around low-mass stars had unique formation pathways. Ho et al. (2024) and Venturini et al. (2024) suggest that the filling in of the radius valley around low-mass stars may point to a dispersion in core-mass fractions due to icy planets or steam worlds, although this scenario is currently indistinguishable from increased photo-evaporative or collisional mass loss for planets around late-type stars.

The metal contents of stars, and specifically of low-mass stars, can be measured in several ways (Passegger et al. 2022). By combining model stellar atmospheres and radiative transfer codes, synthesized spectra can be compared to observations (e.g. Bean et al. 2006; Wanderley et al. 2025). However, this process of spectral synthesis is complicated for M dwarfs due to the high volume of complex molecular features and lack of continuum at optical wavelengths. Several other methods thus make use of supervised machine learning (e.g. Antoniadis-Karnavas et al. 2024; Behmard et al. 2025) and photometric calibrations using FGK-M binary systems (e.g. Bonfils et al. 2005; Duque-Arribas et al. 2023).

Near-infrared (NIR) spectra are commonly used to characterize low-mass stars (e.g. Hejazi et al. 2015; Mann et al. 2013d,a), due to strong metallicity-sensitive features in this wavelength regime as well as enhanced luminosity of cool dwarfs at longer wavelengths. Nevertheless, there remain systematic offsets between different metallicity measurement methods (e.g. Jofré et al. 2019; Pass et al. 2025), highlighting the need for uniformly derived metallicities to make inferences about the planet populations orbiting low-mass stars.

In this paper, we used IRTF/SpeX NIR spectra to characterize 59 cool dwarf stars observed by *TESS* which host confirmed planets or planet candidates. In Section 2, we present our sample and target selection criteria, and we present the observations used in this work in Section 3. We then detail the methods used to measure metallicities and other key stellar parameters from our observations in Section 4. We provide updated planet parameters and vet the 25 planet candidates in our sample in Section 5. Finally, in Section 6 we discuss the relationship between stellar metallicity and planet parameters, and conclude in Section 7.

2. SAMPLE

We selected the targets in our sample from the sample of *TESS* Objects of Interest (TOIs) released and vetted by the *TESS* Science Office¹, with a view to target cool dwarfs with transiting planet candidates or confirmed planets. We first restricted our sample to targets with effective temperatures $< 4000K$ and stellar radii $< 0.75R_{\odot}$, in order to target cool stars in the M and late-K spectral classes. These initial stellar parameters were reported in the *TESS* Input Catalog (TIC v8.2 Paegert et al. 2022). For each star, the stellar radius was calculated using *Gaia* parallaxes and magnitudes. Stellar effective temperatures were calculated using an empirical photometric relation with colour (Stassun et al. 2018). We restricted the sample to targets observable using the IRTF ($-30^{\circ} < \delta < +65^{\circ}$). We then removed fainter stars ($K_{mag} > 13$). We also excluded targets for which the planet candidate radius reported on ExoFOP was greater than $1R_J$; deeper transits are more likely to be False Positives caused by eclipsing binaries. Finally, we prioritized obtaining observations for stars hosting multiple planets or planet candidates and for brighter stars. Our final sample of 59 stars is presented in Table 4.

Within this sample, there are 51 confirmed planets and 25 planet candidates. These planets are quite di-

verse; they range from the size of Venus to that of Jupiter, and their orbital periods range from 0.5 to 48.7 days. Additionally, eight of the planets have measured masses, six of which have radii $< 4R_{\oplus}$. These planets span a range of densities, from $1.8 \pm 0.3g/cm^3$ (GJ 436 b, Maciejewski et al. 2014) to $7.0 \pm 1.2g/cm^3$ (GJ 486 b, Trifonov et al. 2021). Of the 76 planets and planet candidates, 67 have radii $< 4R_{\oplus}$, and 2 have radii similar or greater than that of Saturn² ($9.1R_{\oplus}$).

3. OBSERVATIONS

3.1. IRTF/SpeX

We collected medium-resolution spectra for our targets using the SpeX instrument (Rayner et al. 2003a) on the 3m NASA Infrared Telescope Facility (IRTF) between May 2023 and January 2024. We collected observations using the SXD mode with a $0.3'' \times 15''$ slit, providing a spectral resolution of $R \approx 2000$ over a wavelength range of $0.7 - 2.55 \mu m$ (Rayner et al. 2004). We used exposure times of no more than 180 seconds, and we collected 65 spectra of 59 unique targets.

For each observation, we used an ABBA nod pattern, with the A and B positions on the slit separated by $7''.5$. In this pattern, each pair of images is subtracted, in order to remove the impact of dark and other telescope currents on the images. This approach does not correct for sky background, as this varies between locations A and B. However, we synced the slit to the parallactic angle in order to ensure that atmospheric dispersion occurred along the slit, minimizing light loss. We repeated the ABBA nod pattern with the goal of achieving a S/N of at least 100 per resolution element.

We also acquired observations of A0V stars to use for telluric corrections. We identified the nearest appropriate A0V star to each science target using the SpeX locator tool³. Where possible, we observed A0V stars directly following science observations, and no less than every two hours. We observed standard stars with angular distances and airmass differences no greater than 15° and 0.1, respectively.

After each observation of a science target, or set of science observations in a given area of the sky, we took calibration images using the internal quartz and Thorium-Argon lamp. These images were executed using the IRTF/SpeX calibration macro associated with the SXD observation mode and $0''.3$ slit length.

We reduced our spectra using the *Spextool* reduction pipeline (Cushing et al. 2004). *Spextool* was de-

¹ Available at <https://exofop.ipac.caltech.edu/tess/>

² <https://nssdc.gsfc.nasa.gov/planetary/factsheet/saturnfact.html>

³ Available at https://irtfweb.ifa.hawaii.edu/~spex/find_a0v/

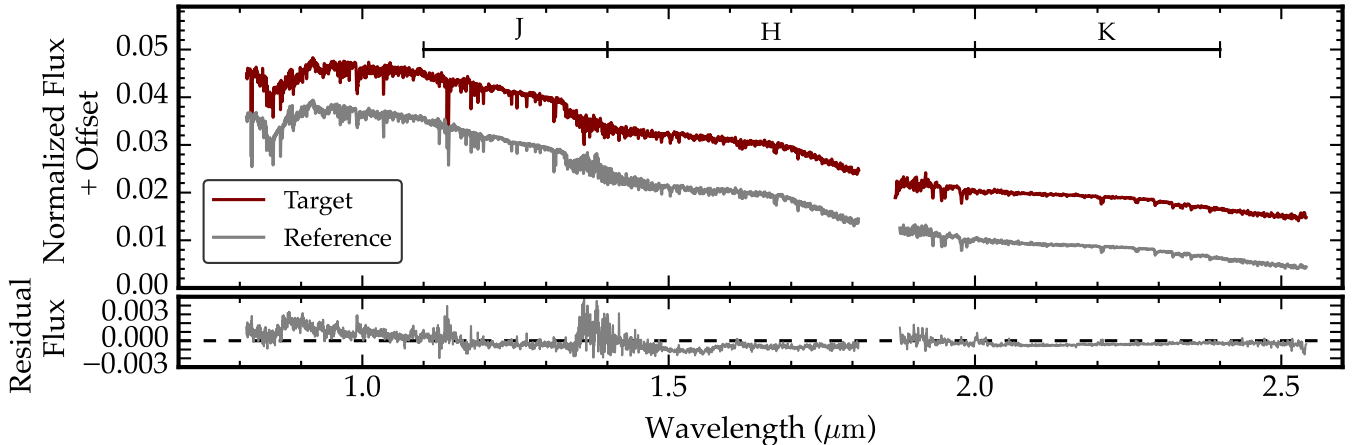


Figure 1. The observed spectrum for TIC 219041246 (TOI-5713, red) compared with a IRTF standard spectrum of Gl 273 (grey). The spectra are offset for visual clarity. The wavelength ranges of the J, H, and K spectral band-passes are indicated for reference. The bottom panel shows the residuals between the observed and standard spectra. The regions of larger residual scatter near $1.4 \mu\text{m}$ are due to high H_2O telluric contamination in those wavelength regimes.

veloped specifically for IRTF/SpEx data, and performs three main steps: calibration frame preparation, spectral extraction, and post-extraction processing of images. Telluric contamination in our spectra was removed using our observations of A0V stars in between science targets and using `xtellcor` (Vacca et al. 2003). We used the calibration and A star images taken nearest to each science target for reduction purposes. We include a representative spectrum in Figure 1.

3.2. Imaging

We incorporate existing imaging observations of 38 of our targets when vetting planets in Section 5.2, in order to rule out nearby eclipsing binaries as false positive scenarios. We describe these observations in the Appendix A.

3.3. Photometry

In order to characterize the planetary systems around our targets, specifically for the 25 targets which host planet candidates (rather than confirmed and/or validated planets), we used photometric observations collected by the Transiting Exoplanet Satellite Survey (TESS, Ricker et al. 2015). We used the two-minute cadence light curves produced by the TESS Science Processing Operations Center (SPOC, Jenkins et al. 2016). The number of sectors observed per target ranged from 1 to 42, with a median of 6 sectors of TESS data per target with a median baseline of 5.2 years.

4. STELLAR CHARACTERIZATION

4.1. Spectroscopic

We followed the methodology of Dressing et al. (2019) and Gore et al. (2024) to measure the stellar masses,

radii, effective temperatures, and metallicities of our targets. We first used the Python implementation⁴ of the `tellrv` package (Newton et al. 2014, 2022) to calculate the absolute radial velocity for each target. We analyzed the J, H, and K bands of each spectrum separately, and cross-correlated each spectrum with the corresponding telluric-corrected standard star (A0V) spectrum. We then calculated the radial velocity of each target by taking the median of the J, H, and K band radial velocities, and shift the science spectrum by this median radial velocity.

Using these shifted lab-frame spectra, we calculated the iron abundance relative to hydrogen ($[\text{Fe}/\text{H}]$) and the total metal abundance relative to hydrogen ($[\text{M}/\text{H}]$). We calculated these metallicities using the relationships for cool dwarfs (spectral types K7 - M5 for $-1.04 < [\text{Fe}/\text{H}] < +0.56$) presented in Mann et al. (2013b). These empirical relations were derived using a sample of 112 wide binary systems with a solar-type primary and cool dwarf secondary. We specifically calculated these metallicities in the J and K-bands of our spectra using the metal-sensitive features centered at 2.2079 , 2.3242 and $2.3844 \mu\text{m}$ identified by Mann et al. (2013b). Önehag et al. (2012) found that J-band derived metallicities are reliable indicators of the metal content of M dwarfs. However, Dressing et al. (2019) argue that K-band metallicities are most reliable for IRTF/SpEx spectra due to increased telluric contamination in the other bands, and we therefore report the K-band-derived metallicities and adopt these values for the remainder of our analysis. The resulting metallic-

⁴ <https://github.com/stevengiacalone/tellrv>

ity measurements have a typical uncertainty of 0.1 dex, and are reported in Table 4. We measure a range of iron abundances ($[\text{Fe}/\text{H}]$: $[-0.57, +0.57]$ dex, median $[\text{Fe}/\text{H}] = -0.03$ dex) and of total metallicity ($[\text{M}/\text{H}]$: $[-0.48, +0.42]$ dex, median $[\text{M}/\text{H}] = -0.04$ dex).

4.2. Photometric

We also calculated the stellar luminosity following the methodology in Dressing et al. (2019). Firstly, we found the r-band magnitude in the Carlsberg Meridian Catalogue (Muiños & Evans 2014), and the V and J magnitudes in the TIC (Paegert et al. 2022). Secondly, we calculated the V-J bolometric correction formula from Mann et al. (2015), incorporating our measured metallicity (specifically, the spectroscopic $[\text{Fe}/\text{H}]$ value) to improve the accuracy of the relation. We added an additional error of 0.012 magnitudes in quadrature to the bolometric correction error to account for scatter in the empirical calculation, as recommended by Mann et al. (2015). Thirdly, we used distances from the TIC to calculate the absolute J-band magnitude (M_J), from which we calculated the stellar luminosity using the bolometric correction.

In order to measure the stellar radius, we used the empirical M_K -radius relation presented in Mann et al. (2015), again incorporating our measured $[\text{Fe}/\text{H}]$ values. We calculated the absolute K magnitude (M_K) for each target using the stellar distance and K magnitude values reported in the TIC. We then calculated the stellar radius, adding an error of 2.7% in quadrature to reflect the scatter in the empirical relation presented in Mann et al. (2015).

We calculated stellar mass using the mass-magnitude relation presented in Mann et al. (2019), adding a systematic uncertainty of $0.02 M_\odot$ in quadrature to reflect the scatter in this empirical relation.

Finally, we calculated the stellar effective temperature using the Stefan-Boltzmann law. The stars in our sample have masses between 0.21 and $0.70 M_\odot$, with a median stellar mass of $0.50 M_\odot$ and standard deviation of $0.12 M_\odot$. The measured effective temperatures range between 3190 and 4600 K, with a median effective temperature of 3650 K and a standard deviation of 260 K, corresponding to early M-type dwarf stars. We report our updated stellar parameters in Table 4, and show the stellar parameter ranges included in our sample in Fig. 2.

5. PLANETS

5.1. Planet Parameters

There are 25 as-yet unconfirmed planet candidates (TESS Objects of Interest, TOIs) orbiting 23 stars in

Table 1. Prior distributions used to fit transits

Parameter	Prior Distribution
$\ln(\text{Orbital Period}), \ln(P)$	$\mathcal{N}(\mu, \sigma = 0.01)$
Transit Epoch, t_0	$\mathcal{N}(\mu, \sigma = 0.1)$
Mean flux, $\langle F \rangle$	$\mathcal{N}(\mu = 1.00, \sigma = 0.01)$
Limb darkening coeff., q_1	$\mathcal{U}(0, 1)$
Limb darkening coeff., q_2	$\mathcal{U}(0, 1)$
Planet-star radius ratio, R_p/R_*	$\mathcal{U}(0.01, 0.3)$
Impact parameter, b	$\mathcal{U}(0, 1 + R_p/R_*)$

our sample. TOIs typically have large radius uncertainties reported on ExoFOP, as the TESS project pipeline takes a generic approach to identifying planet candidates. Therefore, we independently fit the transit data of these TOIs in order to improve the radius measurements. We used the `lightkurve` package (Lightkurve Collaboration et al. 2018) to download the 2-minute SPOC TESS light curves for each of these TOIs. We then normalized and stitched together the light curves from each TESS Sector. For five of the 23 planet candidate hosting TOIs, the TESS mission has collected over 20 sectors of data.

To constrain the size and orbital properties of the planet candidates, we modeled the transit photometry using the `exoplanet` package (Foreman-Mackey et al. 2021). We defined our transit model using the planet-to-star radius ratio (R_p/R_*), transit epoch (T_0), orbital period (P), semi-major axis in units of stellar radii (a/R_*), impact parameter (b), and quadratic limb-darkening coefficients (q_1, q_2 , using the parameterization of Kipping 2013). Our model also included a mean baseline flux term ($\langle F \rangle$). Finally, we assumed a circular orbit for the planets, setting the eccentricity equal to zero.

We optimized the model parameters using Bayesian inference, implementing a Hamiltonian Monte Carlo (HMC) No U-Turn Sampler (NUTS, Hoffman & Gelman 2011) with PyMC3 (Salvatier et al. 2016) to sample the posterior probability distributions. The prior distributions used for each parameter are given in Table 1, and we used the reported ExoFOP planet parameters as test values for each parameter. We set the target acceptance rate to 0.95 (to account for the higher acceptance fractions returned by HMC samplers compared with Metropolis-Hastings samplers) and initialized the sampler by adapting a dense mass matrix from the sample covariances. We then ran the sampler using 2 chains, each drawing 10,000 samples after discarding 2,000 burn-in steps. To check for convergence, we computed the Gelman-Rubin Diagnostic and visually inspected the sampler trace plot for each parameter. The

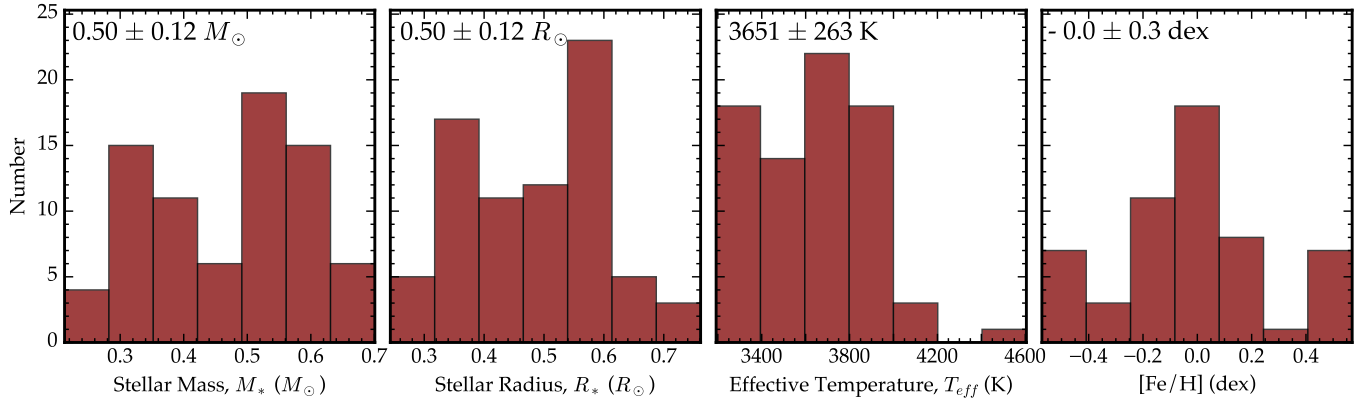


Figure 2. Histograms of measured stellar parameters for the 76 stars in our sample, showing (from left to right) stellar masses, radii, effective temperatures, and metallicities. The median values and associated standard deviations are shown in each panel.

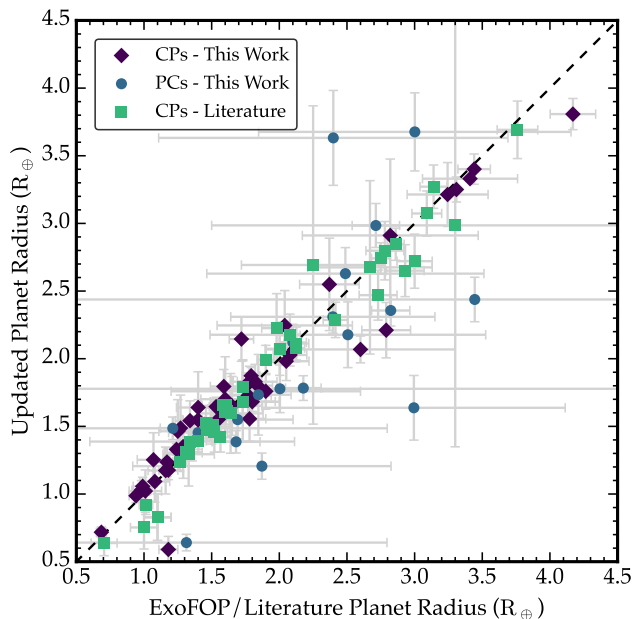


Figure 3. Comparison of existing and updated planet radii for small ($R_p < 4R_\oplus$) planets orbiting M dwarfs. The shape of data points is set by whether the planets’ host stars are in the sample presented in this work (dark purple diamonds - confirmed planets, blue circles - candidate planets) or with existing stellar parameters measured using IRTF/SpeX (green squares). A one-to-one line (dashed black) is included for reference.

median and 68% confidence range for each parameter are given in Table 6.

We used the results of our transit fits (described above) and the measured stellar radii (described in Section 4.2) to calculate updated planet radii. We also recalculated the radii of confirmed planets in our sample using the stellar radii reported in this work and literature planet-to-star radius ratios. We report the orbital periods, planet radii, impact parameters, planet-to-star

radius ratios and times of conjunction in Table 6 for planet candidates and Table 5 for confirmed planets. In Fig. 3, we compare our new radius measurements with existing values from ExoFOP for planet candidates and from the papers referenced in Table 5 for confirmed planets. For the 25 planet candidates, we improved the radius measurement precision for 19 planets, with a median precision improvement of $\sim 80\%$. This improvement is largely driven by the increased precision on the measured transit depths from our fits compared to the transit depths reported on ExoFOP.

5.2. Planet Vetting

Of the 51 confirmed planets in our sample, three have been validated using colour validation (Esparza-Borges et al. 2022; Peláez-Torres et al. 2024). This method depends on the fact that planetary transits are achromatic, while apparent transits due to other astrophysical scenarios (e.g. a blended eclipsing binary) are wavelength-dependent (Rosenblatt 1971; Tingley 2004). Therefore, multi-band photometry of transit events can determine whether they are caused by planets. A further 36 planets have been validated using statistical validation (e.g. Castro González et al. 2020), which compares the observed transit to simulated transits caused by non-planetary phenomena. The remaining planets have been confirmed using radial velocity observations to obtain mass measurements.

For the 25 planet candidates in our sample, we used the *triceratops* (Giacalone et al. 2021) statistical validation Python package to characterize these candidates. This method calculates the probabilities of a range of transit-producing scenarios using the observed transit alongside imaging and photometric observations of the host star to characterize nearby contaminating stars. For this analysis, we folded each light curve to the orbital period and transit epoch of the associated TOI,

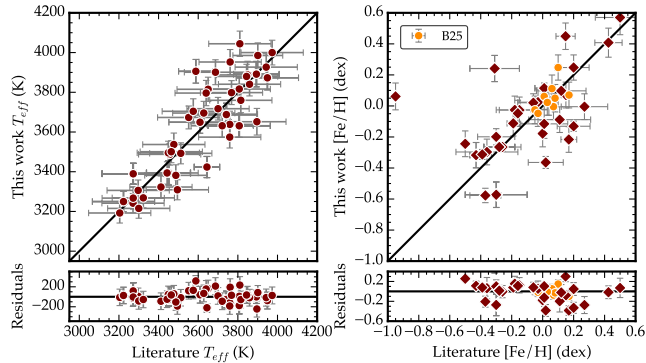


Figure 4. Top: Comparison of literature values from the TIC and measured in this work for stellar effective temperature and metallicity ([Fe/H]). We include a 1:1 line (black) for reference, and highlight stellar metallicity measurements from Behrard et al. (2025, B25) in orange in the right-most plot. The effective temperatures derived from our spectra have markedly smaller errors than the corresponding literature values. Our measured metallicities are in moderate agreement with literature values, with some exceptions discussed in Section 6.1. Bottom: Residuals of our derived values from the catalog measurements. The outliers discussed in Section 6.1 are excluded from the residual plots for visual clarity.

and binned the light curve by a factor of 1200. We also only used the region of the light curve within $\pm P/8$ days of the transit (where P refers to the planet’s orbital period), for computational efficiency. We included the imaging observations described in Section A to identify close stellar companions to the target stars, which would have a diluting effect on the observed transits. We are not able to conclusively validate any of the planet candidates in our sample, but flag five as likely planets (TOIs 233.01, 1638.01, 4325.01, 5511.01, and 5961.01). To do this, we followed the criteria set out in Giacalone et al. (2021), namely that likely planets have false positive probabilities (FPP) < 0.5 and nearby false positive probabilities (NFPP) $< 10^{-3}$. We detail these results in Table 2. We note that the probabilities for each target do not sum to one, as we report the median probabilities after running `triceratops` 20 times on each target.

6. DISCUSSION

6.1. Comparison with Literature Stellar Parameters

Measuring M dwarf stellar properties is notoriously challenging. Their inherent faintness and high activity inhibit photometric characterization, while complex molecular features due to their cool atmospheres hinder spectroscopic studies. Measurements of fundamental stellar properties, namely mass, radius, effective tem-

perature and metallicity, are subject to both intrinsic scatter and systematic errors.

We uniformly measured fundamental stellar parameters of the stars in our sample using IRTF/SpeX spectra, as detailed in Section 4 and reported in Table 4. Our sample is made up of low-mass stars, primarily M dwarfs, with a median stellar mass of $0.50 \pm 0.12 M_{\odot}$ and median effective temperature of 3650 ± 260 K. We measure a range of iron abundances ([Fe/H]) between -0.57 and $+0.57$ dex, and of total metallicity ([M/H]) between -0.48 and $+0.42$ dex.

In Figure 4, we compare our measured stellar parameters with those from the TIC (Paegert et al. 2021). All of the targets in our sample are included in the Cool Dwarf Catalog (CDC, Muirhead et al. 2018; Chittidi et al. 2019), which was incorporated into the the TIC Candidate Target List (CTL) by Stassun et al. (2018, 2019).

Fundamental stellar parameters were measured for targets in the CDC via the following methods, as described in Stassun et al. (2019). Stellar mass was calculated following the mass-magnitude relationship presented in Mann et al. (2019). This is the same relation that we used in Section 4.2 to calculate the masses of our targets. Therefore, the residuals between the literature stellar masses and those reported in this work are, as expected, negligible, and are all consistent with 0 to 1σ . Similarly, stellar radii were measured for CDC targets using the radius-magnitude relation presented in Mann et al. (2015), as we did for the targets presented in this work. However, the CDC stellar radius calculation does not include the [Fe/H] correction that we incorporated. Mann et al. (2015) report that the inclusion of a multiplicative metallicity correction resulted in a small but statistically significant improvement in the resulting radius-magnitude fit.

The effective temperatures of stars in the CDC were calculated using G_{BP} and G_{RP} magnitudes and custom photometric relations based on those reported in Mann et al. (2013c). This relation was developed to calculate effective temperature for stars without measured parallaxes. However, our targets are nearby cool stars with measured distances, and we calculated effective temperature via the Stefan-Boltzmann law (see Section 4.2). We find very good agreement between the literature effective temperatures and those measured in this work. The effective temperature residuals are consistent with 0 for the majority of targets (38/59). We also improve the effective temperature precision by a factor of ~ 2.5 , with the median uncertainty decreasing from 158 K to 59 K.

Table 2. Scenario Probabilities for Likely Planets

TIC	TOI	P (days)	t_0 (BJD-2457000)	Transit Depth (ppm)	P_{TP}	$\sigma_{P_{TP}}$	P_{FPP}	$\sigma_{P_{FPP}}$	P_{NFPP}	$\sigma_{P_{NFPP}}$
415969908	233.01	11.7	1365.26	2780	0.88	0.01	0.24	0.02	0.00	0.00
202185707	4325.01	1.65	1469.37	2710	0.87	0.02	0.26	0.04	0.00	0.00
262689575	5961.01	1.62	2447.79	342	0.96	0.02	0.07	0.05	0.00	0.00
312862941	1638.01	0.92	2908.44	4305	0.87	0.03	0.18	0.03	0.00	0.00
389040826	5511.01	4.72	2575.04	11520	0.94	0.03	0.13	0.06	0.00	0.00

We also compared our measured stellar metallicities with literature values, which were available for 23 of our targets. Behrard et al. (2025, henceforth B25) presented a large catalog of M dwarf metallicities derived using an application of The Cannon (Ness et al. 2015; Casey et al. 2016). This is a data-driven approach of measuring metallicities by training a machine learning model on high-resolution spectra from the Sloan Digital Sky Survey-V/Milky Way Mapper (SDSS-V/MWM, Gunn et al. 2006; Wilson et al. 2019; Kollmeier et al. 2026), with spectra from the Apache Point Observatory Galactic Evolution Experiment (APOGEE, Majewski et al. 2017). The metallicity measurements reported in B25 have an associated uncertainty of 0.02 dex. Ten of the targets in our sample were included in this catalog, and we compared the resulting metallicities in Fig. 4, finding that the $[\text{Fe}/\text{H}]$ values are in moderate agreement, with a few notable outliers. We attribute the moderate differences between our measured metallicities and available literature values as being due to the methods used to calculate $[\text{Fe}/\text{H}]$. The majority of literature metallicities were calculated using ExoFASTv2 (Eastman et al. 2019) to model spectral energy distributions of target stars. This approach uses sparser information than our approach, and therefore returns less reliable metallicity measurements.

K2-344 (TIC 203289099, EPIC 212081533) has a literature stellar metallicity of $[\text{Fe}/\text{H}] = -0.95 \pm 0.02$ dex (de Leon et al. 2021), which is highly discrepant from our measured value of $[\text{Fe}/\text{H}] = 0.06 \pm 0.09$ dex. We attribute this large difference to the use of the kea grid of synthetic stellar spectra (Endl & Cochran 2016) in de Leon et al. (2021) to provide spectroscopic constraints on stellar metallicity. The kea models are calibrated to stars with effective temperatures between 5000 and 6700 K, while K2-244 is a cool dwarf with an effective temperature of 3816 ± 63 K (this work). Therefore, the stellar parameters returned using the kea models are likely inaccurate for this target.

K2-155 (TIC 17307715, EPIC 210897587, LP 415-17, TOI-5562) has a literature stellar metallicity of -0.3 ± 0.2 dex (Díez Alonso et al. 2018a) and mass

of $0.65_{-0.03}^{+0.06} M_{\odot}$, measured using HARPS-N spectra (Cosentino et al. 2012). These values are consistent with those reported in Hirano et al. (2018) ($[\text{Fe}/\text{H}] = -0.42 \pm 0.12$ dex, $M_* = 0.540 \pm 0.056 M_{\odot}$) using the Tull Coudé Spectrograph (Tull et al. 1995) on the McDonald Observatory 2.7m Harlan J. Smith Telescope. In this work, however, we measured a stellar metallicity of -0.57 ± 0.08 dex, which is $\sim 1.5\sigma$ discrepant from the literature values. This difference may be due to the wavelength coverage of the instruments used: HARPS-N and the Tull Coudé Spectrograph are primarily optical instruments compared to the SpeX NIR coverage. Previous work (e.g. Rajpurohit et al. 2018; Johnson & Apps 2009) highlighted possible systematic offsets between optical and IR metallicities, due to complex M dwarf spectra and methodological challenges in obtaining high SNR spectra of a given target in both wavelength regimes.

6.2. Stellar Metallicity – Planet Radius for Small Planets ($R_p < 4R_{\oplus}$)

In order to expand our sample, we identified 28 red dwarfs hosting 43 planets and planet candidates with metallicities measured using IRTF/SpeX spectra and the same methodology as in this paper. These results were published in Dressing et al. (2019) and Gore et al. (2024). By constructing a sample in this way, we avoided introducing systematic errors in metallicities measured using different instruments or techniques. The full sample contained a total of 142 planets and planet candidates orbiting 86 cool dwarf stars. Of these, 108 planets and planet candidates orbiting 72 cool dwarfs had radii $< 4R_{\oplus}$. In Fig. 5, we plotted planet radius as a function of planet instellation and stellar metallicity, showing that cool dwarfs in our sample which host larger planets tend to be metal-rich. The sample also contained seven giant planets, with radii $> 9R_{\oplus}$. As described in Section 5.1, we uniformly re-derived planet radii using stellar radii measured using IRTF/SpeX observations and empirical photometric relations. The stars in the expanded sample span the same stellar mass, radius, and effective temperature ranges as those presented for the first time in this work (see Section 4). We use this expanded sample for the remainder of the discussion.

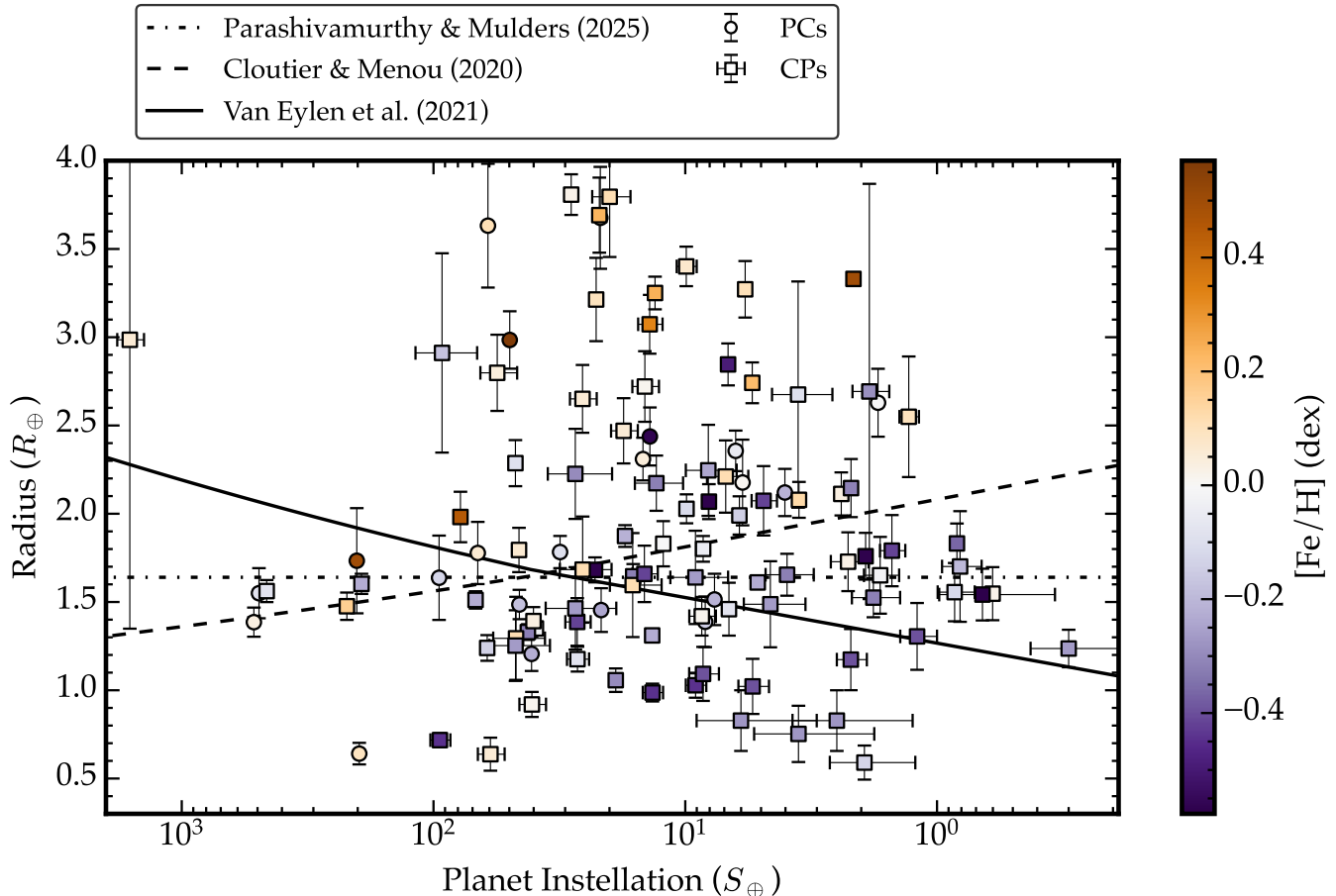


Figure 5. Planet instellation vs. radius for the observed planet candidates (circles) and confirmed planets (squares) in our sample, as well as confirmed planets from the literature (squares). Points are coloured according to measured stellar metallicity $[\text{Fe}/\text{H}]$. Planets orbiting metal-rich stars tend to be larger than those orbiting metal-poor stars. Empirical relations for the radius valley around low-mass stars are shown by solid (Van Eylen et al. 2021), dashed (Cloutier & Menou 2020), and dash-dotted (Parashivamurthy & Mulders 2025) lines, based on completeness-corrected samples of M dwarfs. We note that several of the confirmed planets have substantial uncertainties in planet radius exceeding 20%. These uncertainties are due to large measurement errors in the transit depth reported in the literature (see references in Table 5) and not from the stellar radius uncertainties presented in this study, which are nominal (4%).

Unlike the well-known correlation between giant planet occurrence and stellar metallicity (Fischer & Valenti 2005), the relationship between small planet occurrence and stellar metallicity has not been conclusively settled. Characterizing this relationship is important both for understanding how small planets form, but also to enable conditional occurrence rates which probe how gas giant formation is impacted by the presence or absence of small planets in the system (Bryan & Lee 2025).

Theoretical results suggest that planet formation is broadly suppressed in metal-poor environments (e.g. Mordasini et al. 2012; Burn et al. 2021; Xenos et al. 2025). Wang & Fischer (2015) reported an enhanced occurrence rate for both super-Earths and sub-Neptunes around metal-rich solar-type stars compared to a metal-poor stellar sample. Additionally, Boley et al. (2024)

report evidence of a sharp decrease in small ($1 - 3 R_{\oplus}$) planet occurrence for FGK stars with metallicities lower than $[\text{Fe}/\text{H}] = -0.31 \pm 0.02$ dex. When considering only cool dwarfs, Lu et al. (2020) found a linear relationship between small planet occurrence and stellar metallicity around low-mass stars. They reported that for planets with radii between 2 and $5 R_{\oplus}$, planet occurrence scales linearly with stellar metallicity. They also predicted that planets $< 2R_{\oplus}$ should be very rare around early-type M dwarfs with $[\text{M}/\text{H}] < -0.5$ dex. Conversely, Kutra et al. (2021) find that the occurrence of small Kepler planets ($1 - 4 R_{\oplus}$) is independent of stellar metallicity.

Our sample is consistent with the results suggesting a decreased planet occurrence around the most metal-poor stars, although we do not correct for observational

biases in our sample and so do not calculate occurrence rates. Our sample does not include any planet hosting stars with $[M/H] < -0.5$ dex, and contains only 2 targets with $[Fe/H] < -0.31$ dex. This is in line with the broad picture of planet formation, which requires a sufficient solid mass budget to form planets at all (Lee & Chiang 2015). However, while a measurement of the occurrence of small planets around M dwarfs as a function of stellar metallicity is beyond the scope of this work, we perform an intra-sample comparison of stellar metallicity distributions, described below.

6.3. *Sub-Neptune vs. Super-Earth Host Metallicities*

The cool dwarfs in our sample mostly host planets with radii $< 4R_{\oplus}$, which can further be split into sub-Neptunes and super-Earths. It remains unclear whether super-Earths and sub-Neptunes are formed as distinct populations, and whether these planets form differently around low-mass stars than around solar-type host stars (Parc et al. 2024). Around low-mass stars, super-Earths may primarily be rocky planets that formed in situ (i.e., close in to their host stars where volatiles in the protoplanetary disk are vaporized). In this picture, sub-Neptunes around low-mass stars may be volatile-enriched “water worlds” that formed beyond the ice line and subsequently migrated inwards (Venturini et al. 2020; Schlecker et al. 2021; Alessi et al. 2020; Luque & Pallé 2022; Burn et al. 2024). If the separation between super-Earths and sub-Neptunes is compositional, as evidenced by the empirical density valley around M dwarfs but not FGK stars (Luque & Pallé 2022; Parc et al. 2024), this may be reflected in their host stars’ metallicities. We therefore compare the stellar metallicity distributions between the super-Earth and sub-Neptune hosts in our sample.

In order to split the planet sample into super-Earths and sub-Neptunes, we considered six definitions of the radius valley, three empirical relations and three theoretical relations. We considered a radius cut-off of $1.64 R_{\oplus}$ as reported in Parashivamurthy & Mulders (2025) (henceforth PM25), the negative-slope radius-installation relation of (Cloutier & Menou 2020) (henceforth CM20), and the positive-slope radius-installation relation of (Van Eylen et al. 2021) (henceforth V21). These relations are all empirically motivated for low-mass stars. PM25 derived their radius valley relation using 843 M dwarfs observed by TESS, with a median stellar mass of $0.65 M_{\odot}$. CM20 studied 17,393 early M dwarfs observed by Kepler and K2, with a median stellar mass of $0.67 M_{\odot}$, and V21 considered 27 M dwarfs with well-characterized planets and a median stellar mass of $0.33 M_{\odot}$. The PM25 and C20 samples are well-matched

with ours, which has a median stellar mass of $0.50 \pm 0.12 M_{\odot}$. We note that the radius valley is not visible in our sample (see Fig. 5); this is due to the lack of correction for observational biases in our sample and relatively small planet sample. We constructed our sample by selecting stars with known planet and/or planet candidates. As such, we emphasize that this work does not encompass the underlying planet population or seek to compare the metallicity of planet-hosting stars to those without planets. Rather, we compare the intra-sample metallicity distributions of observed super-Earth and sub-Neptune hosts.

In Fig. 6, we plot the cumulative distribution functions (CDFs) of the stellar metallicities in each subsample. To account for the planet radius and stellar metallicity measurement uncertainties, we calculated the CDFs for the super-Earth and sub-Neptune populations 100 times, sampling the planet radius and $[Fe/H]$ measurements for each planet and corresponding host star. We performed this exercise using the three empirical radius valley scalings discussed above, as well as three theoretical radius valley scalings (see Appendix C). Given that the theoretical scalings do not incorporate a stellar mass dependence, we primarily discuss the results for the empirical radius valley scalings.

The CDFs visually show that the sub-Neptune hosts are typically more metal-rich than the super-Earth hosts for all of the radius valley prescriptions considered. To characterize this observed directionality, we compute the signed difference,

$$\Delta F(x) = F_{\text{SES}}(x) - F_{\text{SNS}}(x), \quad (1)$$

where $F_{\text{SES}}(x)$ and $F_{\text{SNS}}(x)$ are the CDFs evaluated at metallicity x . Positive values of $\Delta F(x)$ indicate that the super-Earth sample contains a larger fraction of objects with $[Fe/H] \leq x$, implying a shift toward lower metallicities relative to the sub-Neptune hosts, while negative values indicate the opposite. We summarize the overall directional offset by integrating the CDF difference, providing a measure of the overall shift in metallicity between the two samples. We find that for all radius valley prescriptions considered, the integrated signed CDF difference is > 0 , demonstrating that the sub-Neptune hosts are typically more metal-rich than the super-Earth hosts. This trend remains when we resampled the population of planets via jack-knife cross-validation, iteratively selecting 80% of the our sample. In order to statistically confirm this distinction in stellar metallicity distributions, we calculated the k-sample Anderson-Darling (AD) test statistic (Scholz & Stephens 1987) for each draw of the sub-Neptune and super-Earth populations. This statistic tests the null hypothesis that

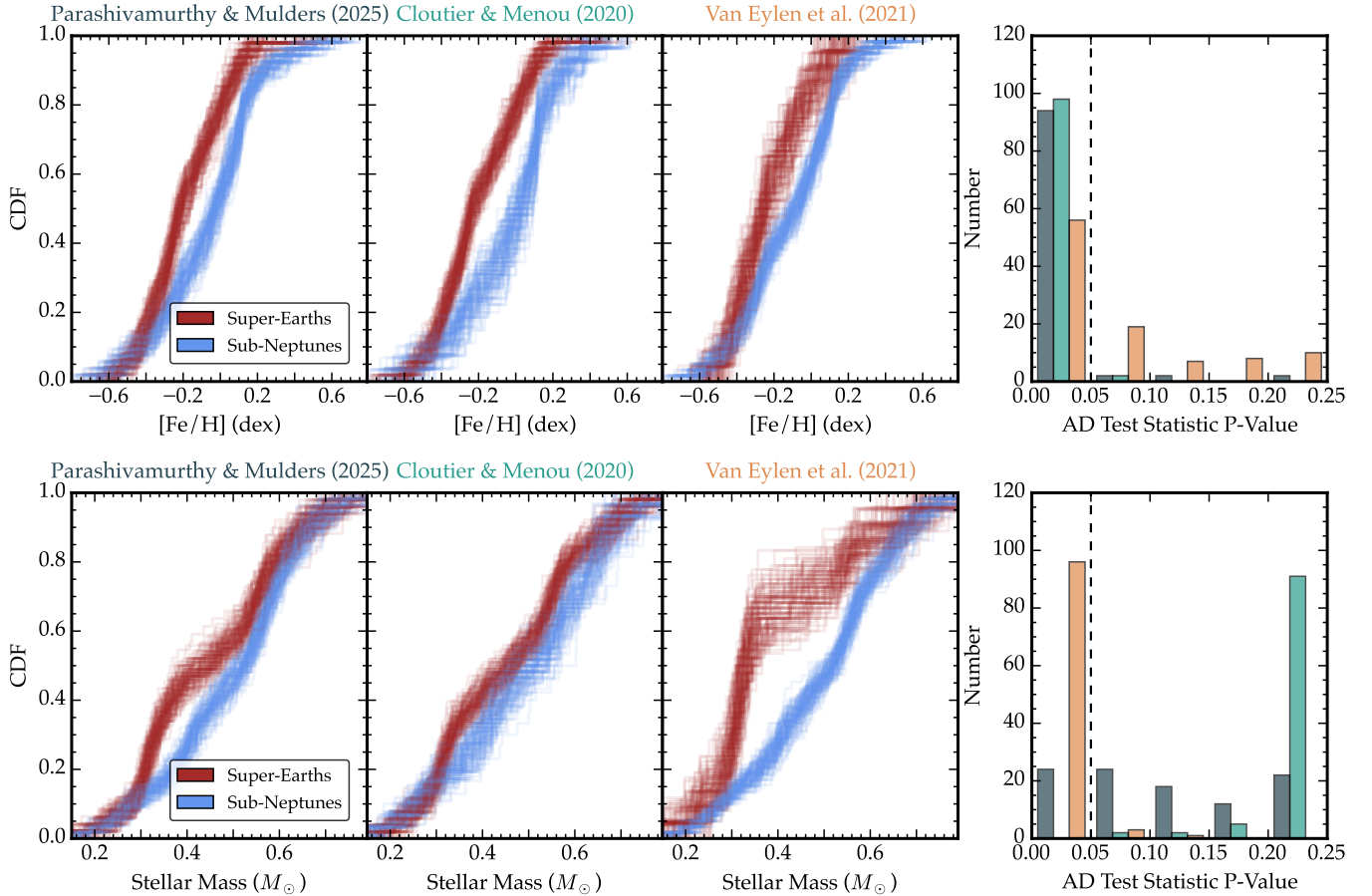


Figure 6. (Left 3 plots:) Per planet cumulative distribution function of measured metallicities (top row) and stellar mass (bottom row) for super-Earths (brown) and sub-Neptunes (blue) for 100 samples of the measured planet radius, stellar metallicity, and stellar mass uncertainties. The distinction between the two populations are set following the empirical radius valley prescriptions from PM25 (dark blue), CM20 (teal), and V21 (orange). (Right:) Histograms showing the p-values associated with the k-sample Anderson-Darling (AD, [Scholz & Stephens 1987](#)) tests for the stellar metallicity (top) and mass (bottom) distributions for each of 100 draws from the planet sample plotted in Fig. 5. A vertical dashed black line at a p-value of 0.05 indicates a typical upper threshold used to reject the null hypothesis under an AD test. These p-value distributions show we can reject the null hypothesis that the stellar metallicity distributions are drawn from the same underlying population with high confidence for the all of the radius valley relations. Additionally, we cannot reject the null hypothesis that the samples are likely drawn from the same stellar mass population for the CM20 radius valley prescription.

metallicity samples are drawn from the same population without needing to specify the form of the underlying distribution. We show the histogram of the p-values associated with these tests in Fig. 6. For the theoretical scalings, we find that the null hypothesis can be rejected more confidently under the gas-depleted formation scenario presented in [Lopez & Rice \(2018\)](#), and can be rejected less frequently for the photo-evaporative mass loss ([Lopez & Rice 2018](#)) and core-powered mass loss ([Gupta & Schlichting 2019](#)) scalings (see Fig. C).

We also investigate whether the observed metallicity enhancement is due to other aspects of the stellar sample. Specifically, we use the AD test statistic to compare the stellar mass, effective temperature, and luminosity distributions of the host stars. We include the corre-

sponding stellar mass CDF plots in Fig. 6 as a representative example. The resulting p-value distributions show that the bulk of the p-values under the CM20 case are > 0.05 , and that we can therefore not reject the null hypothesis that the two stellar mass samples are drawn from the same underlying distribution. We interpret this result as suggesting that the observed metallicity results in the CM20 case are unlikely to be due to differences in the stellar mass, and there is some evidence that this is also the case for the PM25 radius valley definition. However, under the V21 radius valley prescription, we can reject the null hypothesis that the stellar sub-samples are drawn from the same underlying population, with the p-value distribution strongly peaked < 0.05 . This is likely an observational bias, as the V21 radius valley was

constructed using a sample of planets orbiting M dwarfs with well-characterized masses and radii. Super-Earths are typically less massive than sub-Neptunes, and thus are preferentially detected using radial velocities around lower-mass stars, as seen in the stellar mass CDF in the V21 case. Therefore, the observed discrepancy in stellar metallicities in the V21 case is not a robust result. We find the same results for the effective temperature and luminosity CDFs.

In this work, we observe that sub-Neptunes preferentially orbit metal-rich low-mass stars relative to super-Earths. Sub-Neptune formation and interior structure remain open questions. Given the rapid inward drift and accretion of solid material in the inner regions of protoplanetary disks (Ogihara et al. 2015), migration is highly likely to have played a role in shaping the observed population. However, it is unclear where the solid building blocks of sub-Neptunes are primarily assembled (e.g. Johansen & Lambrechts 2017; Bean et al. 2021): solid material may migrate inwards before aggregating into planets (i.e., drift model), or planetary cores may form further out in the disk before experiencing inward migration (i.e., migration model). If sub-Neptunes orbiting M dwarfs are water-worlds, their volatile-rich interiors are most consistent with the migration model, as pebbles migrating inwards would lose their volatile contents prior to assembly under the drift model (Bean et al. 2021; Bitsch et al. 2019; Venturini et al. 2020, 2024).

We note that other mechanisms have been invoked to explain the radius valley around FGK stars, including photo-evaporative mass loss (Owen & Wu 2013), core-powered mass loss (Gupta & Schlichting 2019), gas-depleted formation (Lopez & Rice 2018), and gas-poor formation (Lee et al. 2022). These processes are also able to reproduce the radius valley around FGK stars, and may also lead to distinct stellar metallicity distributions between super-Earth and sub-Neptune host stars. Both photo-evaporative and core-powered mass loss are suppressed in high metallicity atmospheres (Owen & Murray-Clay 2018b; Gupta & Schlichting 2020). If metal-rich stars host planets with higher atmospheric metallicities which thus experience less mass loss, this would also produce the enhanced sub-Neptune occurrence around metal-rich FGK stars (Petigura et al. 2018), and the observed metal-rich sub-Neptune host M dwarfs presented in this work. The gas-depleted and gas-poor formation scenarios also could reproduce this result, as solid cores are able to form more rapidly and thus accrete gas to form sub-Neptunes around metal-rich stars with enhanced metal content in their disks. However, in all of these scenarios, the sub-Neptunes

produced are likely gas dwarfs, with solid cores surrounded by H/He envelopes. This is in conflict with the observed density valley for planets around M dwarfs, which strongly suggests a compositional difference between super-Earths and sub-Neptunes orbiting low-mass stars. Additionally, Cherubim et al. (2023) found that the compositions of seven close-in small planets orbiting M dwarfs disfavor thermally-driven mass-loss mechanisms. Therefore, we consider these mechanisms as less likely to have formed the small planets in our sample, although distinct stellar metallicity distributions alone are not sufficient to discriminate between different formation pathways, and we do not present an occurrence result in this work.

In order to connect the observational trend presented in this work with underlying theories of planet formation, we also consider results from planet population synthesis models. The Next-Generation Planet Population Synthesis model (Emsenhuber et al. 2021) incorporates a diverse set of physical processes, including planetesimal accretion and migration through the disk. Burn et al. (2021) found that planets formed around low-mass stars under this model also display a bimodal density distribution made up of dry, rocky super-Earths and wet sub-Neptunes. They also found that the mean metallicity of low-mass ($M_* < 1M_\odot$) stars hosting sub-Neptunes was higher than that of stars hosting super-Earths. Higher metallicities may be required to form sub-Neptunes around low-mass stars due to the relatively small disk masses and thus small solid reservoirs available for planet formation.

Bitsch & Johansen (2016) found that water-rich planet formation is enhanced in disks with low water-to-silicate ratios. They find that disks with large refractory reservoirs have high Rosseland mean opacities across the disk, unlike water-dominated disks where the opacity decreases inside of the ice line as icy grains sublimate. The increased opacity in low water-to-silicate disks inhibits gas accretion onto protoplanets and thus their subsequent outward migration. This suggests that both the refractory and water content beyond the ice line is important in forming water-rich planets. Therefore, sub-Neptune formation via the accretion of water-rich pebbles beyond the snow line would be enhanced in metal-rich disks. If super-Earth and sub-Neptune cores were primarily made up of refractories (i.e., with limited or no water), we would not expect there to be evidence of distinct host star metallicity distributions. The enhanced metal content of sub-Neptune-hosting M dwarfs presented in this work implies that additional material (namely, water) is involved in sub-Neptune formation around M dwarfs. Future, sensitivity-corrected studies

will enable a demographic study of this topic, teasing apart the occurrences of both super-Earths and sub-Neptunes orbiting M dwarfs as a function of stellar metallicity.

6.4. *Sub-Neptune vs. Super-Earth-Only System Metallicities*

In the previous section, we compare the metallicities of M dwarfs that host super-Earths and sub-Neptunes. There are, of course, M dwarfs that host both super-Earths and sub-Neptunes, or multiple of either type of planet. In our sample there are 19 multi-planet systems, 4 of that host more than 3 planets. These stars which host multiple transiting planets are thus counted repeatedly in the CDFs calculated and shown in Fig. 6. Above, we discuss a formation scenario wherein sub-Neptunes around M dwarfs form in metal-rich disks beyond the ice line prior to inward migration. In this picture, we expect to see a discrepancy between the metallicity distributions of stars which host only super-Earths and stars which host any number of sub-Neptunes, as systems that did not have some critical metal inventory could not have formed any sub-Neptunes.

We plot the CDFs of stellar metallicity on a per system basis in Fig. 7 as opposed to the per planet basis depicted in Fig. 6. In this case, we consider the metallicity distribution of stars hosting at least one super-Earth and strictly no sub-Neptunes (i.e., super-Earth-only systems) and of stars hosting at least one sub-Neptune and any number of super-Earths (i.e., any-sub-Neptune systems). Similarly to Section 6.3, we calculate the integrated signed CDF difference, and find that for all radius valley prescriptions considered, the integrated signed CDF difference is > 0 , demonstrating that the any-sub-Neptune hosts are typically more metal-rich than the super-Earth-only hosts. We observe a significant discrepancy between the super-Earth-only and any-sub-Neptune systems, and are able to reject the null hypothesis that their stellar metallicity distributions are drawn from the same underlying population most confidently under the PM25 and CM20 scenarios using AD tests. We are not able to confidently reject the null hypothesis under the V21 radius valley prescription.

We attribute the discrepancy between the PM25/CM20 results and the V21 result to the differing parameter spaces for which the radius valley relations apply. The sample of M dwarfs used in V21 had a median stellar mass of $0.33 M_{\odot}$, which is lower than our sample’s median mass of $0.49 M_{\odot}$. The radius valley is found at smaller radii for planets around low-mass stars (Cloutier & Menou 2020). Therefore, the V21 radius valley definition may “misclassify” planets in our

sample, which could lead to the statistically weaker distinction between the stellar metallicity distributions of the only-super-Earth and any-sub-Neptune host stars. Furthermore, we perform the same checks as before on the stellar mass, luminosity, and effective temperature distributions. The resulting p-values indicate that the super-Earth-only and any-sub-Neptune host stars are inconsistent with being drawn from the same population under the V21 radius valley definition. For these reasons, we do not consider the higher AD test statistic p-value distributions under the V21 radius valley definition to weaken the observed enhanced metallicity of any-sub-Neptune system host stars under the PM25 and CM20 radius valley definitions.

We observe an enhanced metallicity of sub-Neptune host stars compared to super-Earth-only host stars, and this result is in line with the picture of planet formation discussed in Section 6.3. If sub-Neptunes preferentially form in metal-rich disks, where there is sufficient solid and volatile content beyond the water ice line to form these water-rich planets, if any sub-Neptune is able to form in a given disk, this should not preclude super-Earths forming. However, if we observe a super-Earth-only system, we expect these systems to be more metal-poor than those containing sub-Neptunes. This is borne out in the CDFs computed on a per system basis in Fig. 7 (distinct from the per planet CDFs presented in Fig. 6), albeit at a lower statistical significance than the per-planet result. For the CM20 radius valley definition, we can reject the null hypothesis for the stellar metallicity distributions with p-value < 0.05 in \sim half of the samples. This result thus moderately supports the proposed water-rich formation of sub-Neptunes around low-mass stars. We again note that this discussion is limited to the *observed* planets in our sample, and that future, completeness-corrected studies are needed to probe the true metallicity distributions of super-Earth-only and sub-Neptune planetary systems.

6.5. *Planet Orbital Period*

We also consider the relationship between stellar metallicity and planet orbital period. Wanderley et al. (2025) found that planets with orbital periods < 4.3 d and radii $> 3R_{\oplus}$ preferentially orbit metal-rich M dwarfs. This trend is recovered in this work, but is not a clear result due to the small number (14) of planets with radii $> 3R_{\oplus}$ and periods < 4.3 d in our sample. Similar results for FGK stars (e.g. Mulders et al. 2016) suggest that metal-rich stars may have formed from protostellar disks with enhanced solid fractions, providing a larger reservoir of solids for close-in planet formation. This result, combined with an enhanced surface density of M

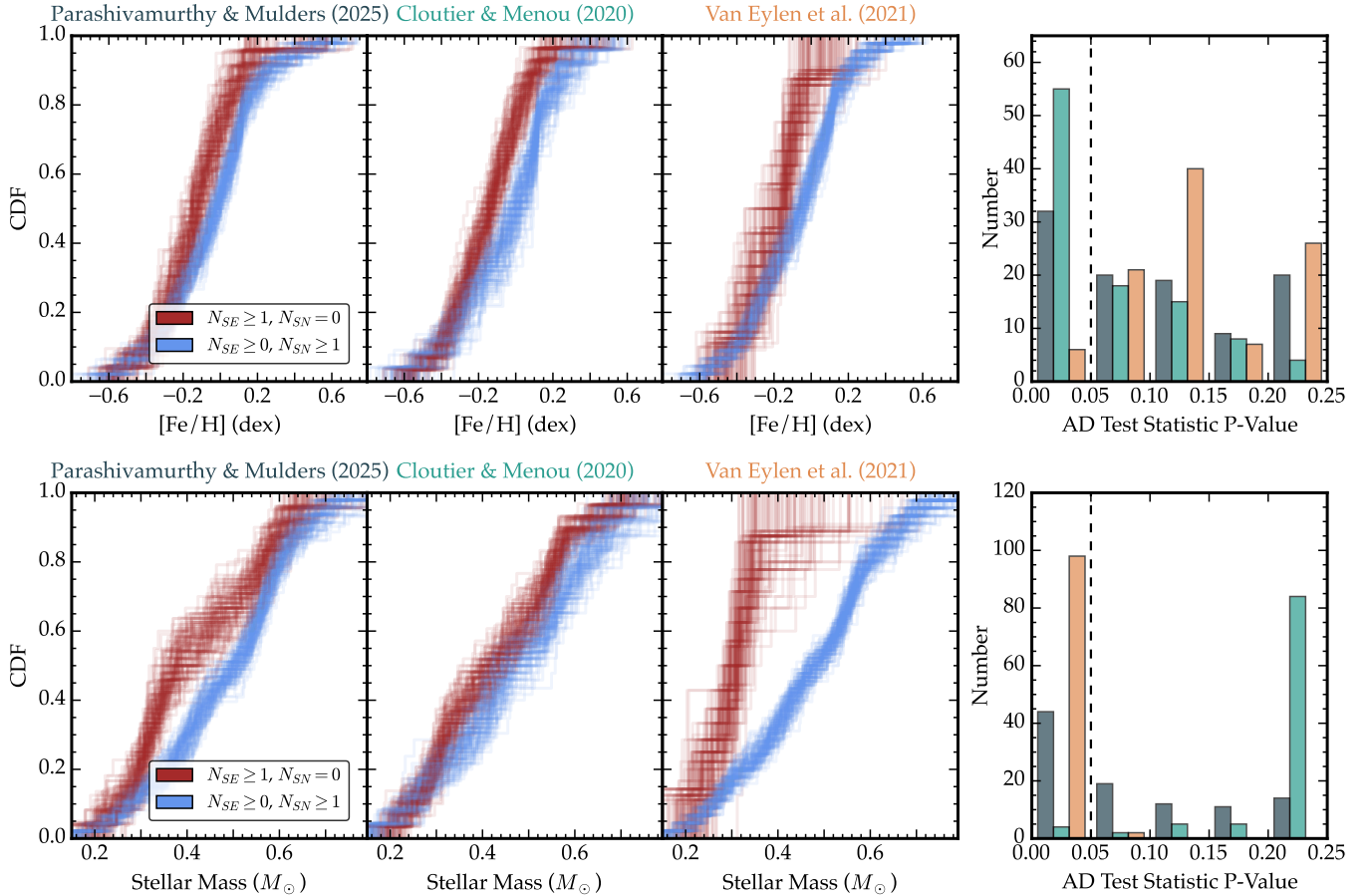


Figure 7. CDFs of stellar metallicity and mass, as in Fig. 6, but plotted on a per system basis rather than a per planet basis. Super-Earth-only systems are shown in brown and any-sub-Neptune systems are shown in blue. The p-value distributions show that we can reject the null hypothesis, namely that the per system stellar metallicity distributions are drawn from the same underlying population, for the PM25 and CM20 radius valley relations. Additionally, we cannot reject the null hypothesis that the stellar mass samples are drawn from the same distribution under the CM20 radius valley prescription.

dwarf disks within 0.5 AU (Gaidos 2017), may explain the apparent abundance of close-in planets orbiting M dwarfs (Ment & Charbonneau 2023).

6.6. Planet Radius for Giant Planets & Brown Dwarfs ($R_p > 9R_{\oplus}$)

The expanded sample discussed in this work contains six substellar objects with radii $> 9R_{\oplus}$, two of which orbit metal-poor stars: HATS-76 b (TIC 170849515, TOI 555, $[\text{Fe}/\text{H}] = -0.17 \pm 0.14$ dex, Gore et al. 2024) and TOI-1278 B (TIC 163539739, $[\text{Fe}/\text{H}] = -0.18 \pm 0.09$ dex, Gore et al. 2024).

While giant planets are typically rare around low-mass stars (Bryant et al. 2023), they appear to exhibit the same stellar metallicity dependence as those orbiting FGK stars. Giant planets mostly orbit metal-rich low-mass stars (Chachan et al. 2025; Gan et al. 2025). This result is consistent with close-in giant planets forming via core accretion followed by a runaway gas accretion

phase, which is enhanced in metal-rich protoplanetary disks (Ida & Lin 2004).

HATS-76 b was confirmed by Jordán et al. (2022a), who reported a stellar metallicity of 0.29 ± 0.13 dex using NIR spectra from ARCoIRIS on the Blanco 4-m telescope (Abbott et al. 2016). This is $\sim 3\sigma$ discrepant from the metallicity reported in Gore et al. (2024) ($[\text{Fe}/\text{H}] = -0.17 \pm 0.14$ dex). This may be due to the SNR of the spectra used to calculate metallicity in both cases; the relations presented in Newton et al. (2014) were calculated using spectra with $\text{SNR} > 200$, far exceeding the SNR of 40 spectrum used in Jordán et al. (2022a). The spectrum of HATS-76 used in Gore et al. (2024) had an SNR of 80, also somewhat lower than the SNR ~ 100 spectra used to develop the Mann et al. (2013c) relations. The large discrepancy between the reported metallicities may thus be due to low spectral quality, or to systematic offsets between the methods used to measure metallicity.

Unlike giant planets, brown dwarfs do not form more readily around metal-rich stars, pointing to a distinct formation pathway such as gravitational instability (Boss 1997; Chabrier et al. 2014; Bowler et al. 2020). Schlaufman (2018) found that close-in ($a < 0.25$ AU) objects with masses $> 10M_J$ orbit stars with a distinct stellar metallicity distribution from less massive giant planets. Artigau et al. (2021a) found that TOI-1278 B is in fact a transiting brown dwarf with a mass of $18.5 \pm 0.5 M_J$ orbiting the MOV star TOI-1278, using the SPIRou instrument on the 3.6 m Canada-France-Hawaii Telescope (Donati et al. 2020). Given this context, our measured metallicity of -0.18 ± 0.09 dex is not surprising.

7. CONCLUSIONS

In this work, we measured metallicities for 59 cool dwarf stars which host confirmed planets or planet candidates. By obtaining NIR spectra using IRTF/SpeX, we determined that the stars in our sample had metallicities ($[Fe/H]$) ranging from -0.6 to + 0.6 dex with a median metallicity of 0.0 dex. Combining our sample of newly characterized candidate and confirmed planet host stars with existing literature, we created a sample of 142 planets and planet candidates orbiting 86 cool, low-mass stars with homogeneously derived stellar parameters. We studied whether the M dwarfs hosting super-Earths and sub-Neptunes had distinct metallicity distributions. We found that cool dwarfs hosting sub-Neptunes were typically more metal-rich than those hosting super-Earths (median $[Fe/H]_{SN} = 0.05$ dex, $[Fe/H]_{SE} = -0.14$ dex, $\sigma_{[Fe/H]} = 0.2$ dex). This result is in line with sub-Neptunes around low-mass stars forming in water-rich environments beyond the snow line before migrating inwards to their observed locations. Protoplanetary disks around metal-rich M dwarfs have higher solid contents than metal-poor disks, providing both the inventory of ices and refractory elements needed to form sub-Neptunes in outer disk regions.

The authors wish to recognize and acknowledge the very significant cultural role that the summit of Maunakea has within the indigenous Hawaiian community. We are most fortunate to have the opportunity to conduct observations from this sacred mountain which is now colonized land. We also thank E. Gillis, N. Gromek, I. Malsky, R. Pudritz, and D. Weisserman for insightful discussions.

This research has made use of the Exoplanet Follow-up Observation Program ([ExoFOP 2019](#)) website, which is operated by the California Institute of Technology, under contract with the National Aeronautics and Space Administration under the Exoplanet Exploration Program. This paper presented data collected by observing with the Infrared Telescope Facility (IRTF), which is operated by the University of Hawaii under contract 80HQTR24DA010 with the National Aeronautics and Space Administration. This paper made use of data collected by the *TESS* mission and are publicly available from the Mikulski Archive for Space Telescopes (MAST) operated by the Space Telescope Science Institute ([Paegert et al. 2022](#); [TESS Team 2018](#)). Funding for the *TESS* mission is provided by NASA’s Science Mission Directorate. We acknowledge the use of public *TESS* data from pipelines at the *TESS* Science Office and at the *TESS* Science Processing Operations Center. Resources supporting this work were provided by the NASA High-End Computing (HEC) Program through the NASA Advanced Supercomputing (NAS) Division at Ames Research Center for the production of the SPOC data products. This research has made use of NASA’s Astrophysics Data System, and of the NASA Exoplanet Archive ([NASA Exoplanet Archive 2019](#)).

SG is supported by an NSF Astronomy and Astrophysics Postdoctoral Fellowship under award AST-2303922.

Facilities: IRTF/SpeX ([Rayner et al. 2003b](#)), *TESS* ([Ricker et al. 2015](#))

Software: `numpy` ([Harris et al. 2020](#)), `astropy` ([Astropy Collaboration et al. 2013, 2018, 2022](#)), `pandas` ([Wes McKinney 2010](#); [pandas development team 2020](#)), `astroquery` ([Ginsburg et al. 2019](#)), `lightkurve` ([Lightkurve Collaboration et al. 2018](#)), `tellrv` ([Newton et al. 2022](#)), `matplotlib` ([Hunter 2007](#)), `exoplanet` ([Agol et al. 2020](#); [Kumar et al. 2019](#); [Foreman-Mackey et al. 2021](#); [Luger et al. 2019](#); [Salvatier et al. 2016](#); [Theano Development Team 2016](#); [Foreman-Mackey et al. 2021](#)), `Spextool` ([Cushing et al. 2004](#); [Vacca et al. 2003](#))

APPENDIX

A. IMAGING OBSERVATIONS

In this section we review the imaging observations of our targets, as executed by members of the *TESS* Follow-up Observing Program Working Group Sub-Group 3 (SG3). This sub-group conducts high-resolution imaging of TOIs, using adaptive optics, speckle imaging, and/or lucky imaging on a variety of instruments. The aim of SG3 is to detect nearby objects that are not resolved in the *TESS* Input Catalog or by seeing-limited photometry. Of our sample, 34 targets have imaging observations. Several targets have multiple imaging observations; we make use of the observations taken in the reddest filter in each case. The spectral energy distributions of cool stars, such as those in our sample, are more similar at longer wavelengths than in the optical. As a result, their magnitudes are also more similar, and therefore more likely to be detectable in a given contrast curve. Each of the contrast curves that we use are available to download on ExoFOP-*TESS* ⁵, and we summarized the observations used in Table 3.

Table 3. Summary of High-Resolution imaging observations used in Section 5.2. An asterisk (*) denotes the filter used in the vetting analysis when multiple were available.

TIC ID	TOI	Instrument	Telescope	Date	Filters	Contrast at 0.5'' [mag]	Companions
415969908	233	'Alopeke	Gemini-N	12 September 2019	562, 832* nm	4.95, 6.25	None
312862941	1638	'Alopeke	Gemini-N	03 December 2020	562, 832* nm	4.68, 5.83	None
232635922	1745	PHARO	Palomar	24 August 2021	Br γ *	5.877	$\Delta\text{mag} = 3.75 \pm 0.02$, $\theta = 1.003''$, PA = $10^\circ \pm 1^\circ$
332477926	1754	NESSI	WIYN	25 April 2021	562, 832* nm	4.372	None
138762614	1802	NIRC2	Keck-II	28 May 2020	Br γ	7.34	None
166648874	1806	PHARO	Palomar	05 December 2020	Br γ	4.779	None
321669174	2081	PHARO	Palomar	19 March 2022	Br γ	6.213	None
243313296	2278	PHARO	Palomar	24 August 2021	H-cont, Br γ *	6.952, 6.968	None
405763009	2433	PHARO	Palomar	19 September 2021	Br γ	7.122	None
59128183	2453	PHARO	Palomar	24 February 2021	Br γ	6.968	None
202185707	4325	PHARO	Palomar	19 March 2022	Br γ	6.169	None
337385330	5112	PHARO	Palomar	19 March 2022	Br γ	6.434	None
389040826	5511	Zorro	Gemini-S	03 January 2024	562, 832* nm	4.68, 5.74	None
443582629	5519	NESSI	WIYN	25 April 2021	562, 832* nm	4.00, 4.84	None
422217860	5662	PHARO	Palomar	19 September 2021	H-cont, K-cont*	7.093, 6.716	None
310380289	5736	NIRC2	Keck-II	10 June 2023	K-cont	7.345	None
262689575	5961	Zorro	Gemini-S	04 July 2023	562, 832* nm	5.02, 6.55	None
354173595	5974	NIRC2	Keck-II	05 August 2023	J, K-cont*	6.916, 7.860	None
120045750	5981	PHARO	Palomar	29 June 2023	Br γ	7.129	None
284900292	5987	PHARO	Palomar	01 July 2023	Br γ	6.62	None
196066560	6077	PHARO	Palomar	29 June 2023	H-cont, Br γ *	6.280, 6.661	None

B. STELLAR & PLANET PARAMETERS

In this section we include Table 4 detailing the stellar parameters measured using IRTF/SpeX spectra for the 76 stars in our sample. We also include Tables 5 and 6, which detail the planet parameters resulting from photometric fits for the confirmed planets and planet candidates in our sample, respectively.

⁵ <https://exofop.ipac.caltech.edu/tess/>

Table 4. Updated stellar parameters using IRTF/SpeX spectra

ID	TOI	Other Names	R_* (R_\odot)	M_* (M_\odot)	L_* (L_\odot)	$\log(g)$ (dex)	T_{eff} (K)	[Fe/H] (dex)	[M/H] (dex)
16005254	5344		0.57 ± 0.02	0.57 ± 0.02	0.0553 ± 0.0002	4.68 ± 0.03	3704 ± 63	0.41 ± 0.09	0.24 ± 0.09
17307715	5562	K2-155, LP 415-17	0.59 ± 0.02	0.57 ± 0.02	0.0721 ± 0.0025	4.65 ± 0.03	3891 ± 64	-0.57 ± 0.08	-0.45 ± 0.08
18318288	6086		0.26 ± 0.01	0.23 ± 0.02	0.0064 ± 0.0002	4.97 ± 0.05	3215 ± 50	-0.09 ± 0.08	-0.09 ± 0.08
19028197	5094	GJ 3470, Kaewkosin ^a	0.49 ± 0.01	0.5 ± 0.02	0.0399 ± 0.0011	4.75 ± 0.03	3673 ± 58	0.25 ± 0.08	0.12 ± 0.08
26054627	5349		0.57 ± 0.02	0.58 ± 0.02	0.0607 ± 0.0021	4.69 ± 0.03	3796 ± 64	0.57 ± 0.11	0.27 ± 0.11
48353358	6004	KIC 10905746, KOI-1725, Kepler-1651 A	0.49 ± 0.01	0.49 ± 0.02	0.0382 ± 0.0018	4.74 ± 0.03	3638 ± 66	-0.05 ± 0.08	-0.09 ± 0.08
59128183	2453		0.5 ± 0.01	0.5 ± 0.02	0.0398 ± 0.001	4.74 ± 0.03	3649 ± 56	0.1 ± 0.09	-0.01 ± 0.09
67646988	1779		0.3 ± 0.01	0.28 ± 0.02	0.009 ± 0.0002	4.94 ± 0.04	3248 ± 50	0.57 ± 0.09	0.42 ± 0.09
77156829	696	LHS 1678 A	0.35 ± 0.01	0.32 ± 0.02	0.0142 ± 0.0006	4.87 ± 0.04	3393 ± 62	-0.45 ± 0.09	-0.36 ± 0.08
102734241	6002		0.24 ± 0.01	0.21 ± 0.02	0.0061 ± 0.0002	4.99 ± 0.05	3267 ± 56	-0.03 ± 0.09	-0.02 ± 0.09
119584412	1801	HIP 57099, LP 375-23	0.55 ± 0.02	0.54 ± 0.02	0.0538 ± 0.0018	4.7 ± 0.03	3760 ± 62	-0.11 ± 0.08	-0.14 ± 0.08
120045750	5981	KIC 3932730	0.54 ± 0.01	0.54 ± 0.02	0.0452 ± 0.0015	4.71 ± 0.03	3631 ± 59	0.05 ± 0.08	0.05 ± 0.08
126606859	4479		0.43 ± 0.01	0.42 ± 0.02	0.0249 ± 0.0009	4.8 ± 0.03	3495 ± 59	-0.18 ± 0.09	-0.15 ± 0.08
138762614	1802		0.58 ± 0.02	0.57 ± 0.02	0.066 ± 0.0017	4.67 ± 0.03	3841 ± 59	0.01 ± 0.08	-0.03 ± 0.08
138819293	1796	GJ 436, HIP 57087, LHS 310, Noquisi ^b	0.42 ± 0.01	0.42 ± 0.02	0.024 ± 0.0007	4.81 ± 0.03	3488 ± 55	0.02 ± 0.08	-0.03 ± 0.08
166648874	1806		0.39 ± 0.01	0.39 ± 0.02	0.0183 ± 0.0005	4.84 ± 0.03	3390 ± 53	0.5 ± 0.09	0.35 ± 0.09
196066560	6077		0.66 ± 0.02	0.63 ± 0.02	0.0951 ± 0.003	4.6 ± 0.03	3952 ± 63	-0.13 ± 0.08	-0.11 ± 0.08
198385543	1846		0.42 ± 0.01	0.4 ± 0.02	0.0231 ± 0.0006	4.81 ± 0.03	3493 ± 53	-0.22 ± 0.08	-0.17 ± 0.08
202185707	4325		0.45 ± 0.01	0.45 ± 0.02	0.0326 ± 0.0015	4.78 ± 0.03	3652 ± 67	0.11 ± 0.09	0.02 ± 0.09
203289099	5111	EPIC 212081533, K2-244	0.56 ± 0.02	0.55 ± 0.02	0.0595 ± 0.002	4.69 ± 0.03	3816 ± 63	0.06 ± 0.09	0.0 ± 0.09
219041246	5713		0.29 ± 0.01	0.27 ± 0.02	0.0085 ± 0.0002	4.93 ± 0.04	3242 ± 49	0.02 ± 0.08	0.03 ± 0.08
232635922	1745		0.43 ± 0.01	0.42 ± 0.02	0.0278 ± 0.0007	4.78 ± 0.03	3574 ± 55	-0.56 ± 0.09	-0.48 ± 0.09
243313296	2278		0.33 ± 0.01	0.3 ± 0.02	0.0117 ± 0.0004	4.89 ± 0.04	3323 ± 56	-0.23 ± 0.09	-0.2 ± 0.09
262689575	5961	HIP 114941	0.62 ± 0.02	0.61 ± 0.02	0.0868 ± 0.0027	4.64 ± 0.03	3985 ± 63	0.09 ± 0.08	0.04 ± 0.08
277833995	5524	EPIC 248480671, K2-321	0.58 ± 0.02	0.58 ± 0.02	0.0635 ± 0.0019	4.68 ± 0.03	3815 ± 61	0.45 ± 0.09	0.31 ± 0.08
284900292	5987		0.62 ± 0.02	0.61 ± 0.02	0.0823 ± 0.0033	4.64 ± 0.03	3927 ± 67	-0.01 ± 0.09	-0.06 ± 0.08
307809773	4599	BD+17 1320, GJ 239, HD 260655, HIP 31635, LHS 1858	0.47 ± 0.01	0.46 ± 0.02	0.0348 ± 0.0011	4.76 ± 0.03	3631 ± 59	-0.32 ± 0.08	-0.27 ± 0.08
310380289	5736		0.58 ± 0.02	0.57 ± 0.02	0.0681 ± 0.0019	4.67 ± 0.03	3873 ± 61	-0.08 ± 0.08	-0.09 ± 0.08
312862941	1638		0.69 ± 0.02	0.66 ± 0.02	0.1161 ± 0.0035	4.58 ± 0.03	4044 ± 64	0.12 ± 0.08	0.06 ± 0.08
321669174	2081		0.52 ± 0.01	0.51 ± 0.02	0.045 ± 0.0012	4.72 ± 0.03	3688 ± 57	-0.24 ± 0.08	-0.22 ± 0.08
332477926	1754		0.59 ± 0.02	0.58 ± 0.02	0.0723 ± 0.0031	4.66 ± 0.03	3887 ± 69	-0.06 ± 0.08	-0.1 ± 0.08
337385330	5112		0.61 ± 0.02	0.59 ± 0.02	0.0848 ± 0.0022	4.65 ± 0.03	4000 ± 62	-0.1 ± 0.09	-0.11 ± 0.09
348755728	1883		0.49 ± 0.01	0.49 ± 0.02	0.034 ± 0.001	4.75 ± 0.03	3537 ± 58	0.08 ± 0.1	0.03 ± 0.09
354173595	5974		0.37 ± 0.01	0.36 ± 0.02	0.0166 ± 0.0005	4.85 ± 0.03	3382 ± 53	-0.18 ± 0.08	-0.19 ± 0.08
368287008	2015		0.32 ± 0.01	0.3 ± 0.02	0.0104 ± 0.0003	4.91 ± 0.04	3250 ± 51	0.24 ± 0.08	0.19 ± 0.08
387974148	5551	Gar ^c , GJ 486, HIP 62452, LHS 341	0.55 ± 0.02	0.55 ± 0.02	0.0566 ± 0.0017	4.7 ± 0.03	3798 ± 60	0.06 ± 0.09	0.01 ± 0.08
389040826	5511		0.51 ± 0.01	0.51 ± 0.02	0.044 ± 0.0013	4.73 ± 0.03	3695 ± 59	0.05 ± 0.09	0.01 ± 0.09
390651552	1827		0.33 ± 0.01	0.31 ± 0.02	0.0119 ± 0.0003	4.89 ± 0.04	3306 ± 52	-0.03 ± 0.08	-0.04 ± 0.08

Table 4 continued

Table 4 (continued)

ID	TOI	Other Names	R_* (R_\odot)	M_* (M_\odot)	L_* (L_\odot)	$\log(g)$ (dex)	T_{eff} (K)	[Fe/H] (dex)	[M/H] (dex)
405763009	2433		0.31 ± 0.01	0.29 ± 0.02	0.0099 ± 0.0002	4.91 ± 0.04	3268 ± 50	-0.06 ± 0.08	-0.06 ± 0.08
407591297	5388		0.32 ± 0.01	0.29 ± 0.02	0.0109 ± 0.0002	4.9 ± 0.04	3309 ± 50	-0.3 ± 0.08	-0.26 ± 0.08
417931300	2068		0.54 ± 0.02	0.54 ± 0.02	0.0504 ± 0.0012	4.7 ± 0.03	3717 ± 57	-0.0 ± 0.08	-0.02 ± 0.08
422217860	5662		0.6 ± 0.02	0.61 ± 0.02	0.076 ± 0.0023	4.66 ± 0.03	3901 ± 63	0.56 ± 0.08	0.38 ± 0.08
434116397	5955	HIP 116907	0.59 ± 0.02	0.58 ± 0.02	0.0706 ± 0.0021	4.66 ± 0.03	3880 ± 61	0.03 ± 0.08	-0.03 ± 0.08
434226736	5095	EPIC 210490365, K2-25	0.29 ± 0.01	0.27 ± 0.02	0.0079 ± 0.0002	4.94 ± 0.04	3192 ± 51	0.07 ± 0.08	-0.03 ± 0.08
443582629	5519		0.37 ± 0.01	0.35 ± 0.02	0.0162 ± 0.0005	4.85 ± 0.04	3394 ± 56	-0.15 ± 0.08	-0.16 ± 0.08
441420236	2221	HD 197481, AU Mic, GJ 803, HIP 102409	0.68 ± 0.02	0.66 ± 0.02	0.0978 ± 0.0024	4.59 ± 0.03	3906 ± 60	0.11 ± 0.08	0.07 ± 0.08
388804061	5555	K2-18	0.44 ± 0.01	0.44 ± 0.02	0.0264 ± 0.0008	4.79 ± 0.03	3501 ± 55	0.1 ± 0.08	0.05 ± 0.08
173103335	5146	K2-3	0.56 ± 0.02	0.55 ± 0.02	0.056 ± 0.0016	4.69 ± 0.03	3767 ± 59	-0.26 ± 0.08	-0.24 ± 0.08
38337202	-	K2-72	0.33 ± 0.01	0.31 ± 0.02	0.0135 ± 0.0004	4.88 ± 0.04	3400 ± 55	-0.39 ± 0.1	-0.3 ± 0.1
82050863	-	K2-9	0.33 ± 0.01	0.3 ± 0.02	0.0109 ± 0.0004	4.89 ± 0.04	3266 ± 57	-0.22 ± 0.09	-0.18 ± 0.09
27187450	-	KOI 2626, Kepler-1652	0.41 ± 0.05	0.39 ± 0.05	0.0218 ± 0.0073	4.82 ± 0.11	3481 ± 351	-0.2 ± 0.1	-0.16 ± 0.1
239275865	-	KOI 463, Kepler 560 B	0.41 ± 0.01	0.4 ± 0.02	0.0222 ± 0.0008	4.81 ± 0.03	3474 ± 59	-0.31 ± 0.09	-0.25 ± 0.09
268159861	-	KOI 571, Kepler 186	0.55 ± 0.02	0.54 ± 0.02	0.0556 ± 0.0018	4.69 ± 0.03	3769 ± 61	-0.26 ± 0.08	-0.21 ± 0.08
273373582	-	KOI 2418, Kepler 1229	0.56 ± 0.02	0.56 ± 0.02	0.0601 ± 0.0024	4.68 ± 0.03	3807 ± 67	0.02 ± 0.1	-0.04 ± 0.1
122450207	-	KOI 3010, Kepler 1410	0.52 ± 0.03	0.52 ± 0.03	0.0505 ± 0.0085	4.71 ± 0.06	3778 ± 199	-0.12 ± 0.12	-0.07 ± 0.12
158989438	-	KOI 3497, Kepler 1512	0.34 ± 0.05	0.31 ± 0.06	0.0191 ± 0.0071	4.88 ± 0.16	3708 ± 443	-0.13 ± 0.09	-0.14 ± 0.09
28090925	-	KOI 4036, Kepler 1544	0.76 ± 0.02	0.7 ± 0.02	0.235 ± 0.0088	4.52 ± 0.03	4605 ± 77	-0.36 ± 0.09	-0.3 ± 0.09
120499135	-	KOI 4742, Kepler 442	0.69 ± 0.02	0.64 ± 0.02	0.1301 ± 0.004	4.57 ± 0.03	4179 ± 68	-0.58 ± 0.09	-0.43 ± 0.09
415969908	233	LP 821-31	0.38 ± 0.01	0.37 ± 0.02	0.0182 ± 0.0005	4.84 ± 0.03	3424 ± 53	-0.21 ± 0.08	-0.18 ± 0.08

^aName assigned by the IAU NameExoWorlds Program. "Kaewkosin" refers to the crystals of the Hindu deity Indra in the Thai language.

^bName assigned by the IAU NameExoWorlds Program. "Noquisi" means "star" in the Cherokee language.

^cName assigned by the IAU NameExoWorlds Program. "Gar" means "flame" in the Basque language.

Table 5. Updated planet parameters for confirmed planets

TIC	Planet Name	P_{orb} (d)	σ_P (d)	T_c (BJD)	σ_{T_c} (BJD)	b	σ_b	R_p/R_*	σ_{R_p/R_*}	R_p (R_{\oplus})	σ_{R_p} (R_{\oplus})	Stellar Reference	Planet Reference
203289099	* K2-344 b	3.3558500	0.0000920	2458095.74773	0.00126	0.410	0.305	0.0295	0.0014	1.79	0.13	This Work	de Leon et al. (2021)
138819293	GJ 436 b	2.6438831	0.0000006	2454510.80162	0.00007	0.736	0.042	0.0822	0.0011	3.81	0.12	This Work	Maciejewski et al. (2014)
434226736	K2-25 b	3.4845641	0.0000006	2458515.64206	0.00010	0.628	0.035	0.1075	0.0018	3.40	0.11	This Work	Steffansson et al. (2020)
17307715	K2-155 b	6.3420000	0.0020000	2457818.71530	0.00210	0.340	0.235	0.0261	0.0009	1.68	0.07	This Work	Díez Alonso et al. (2018a)
17307715	K2-155 c	13.8500000	0.0060000	2457814.56430	0.00250	0.450	0.340	0.0321	0.0013	2.07	0.10	This Work	Díez Alonso et al. (2018a)
17307715	K2-155 d	40.7180000	0.0050000	2457782.83240	0.00480	0.440	0.315	0.0273	0.0018	1.76	0.13	This Work	Díez Alonso et al. (2018a)
277833995	* K2-321 b	2.2979749	0.0000018	2458141.26759	0.00066	0.470	0.310	0.0315	0.0017	1.98	0.14	This Work	Castro González et al. (2020)
390651552	GJ 486 b	1.4671213	0.0000003	2459939.07160	0.00001	0.120	0.081	0.0372	0.0001	1.35	0.04	This Work	Trifonov et al. (2021)
77156829	LHS 1678 b	0.8602325	0.0000012	2458998.15553	0.00071	0.210	0.150	0.0191	0.0008	0.72	0.04	This Work	Silverstein et al. (2022)
77156829	LHS 1678 c	3.6942840	0.0000046	2458998.45607	0.00061	0.440	0.115	0.0262	0.0011	0.99	0.05	This Work	Silverstein et al. (2022)
307809773	HD 260655 b	2.7695300	0.0000300	2459497.91020	0.00040	0.665	0.023	0.0259	0.0005	1.33	0.04	This Work	Luque et al. (2022a)
307809773	HD 260655 c	5.7058800	0.0000700	2459490.36460	0.00040	0.830	0.007	0.0320	0.0010	1.65	0.07	This Work	Luque et al. (2022a)
126606859	* TOI-4479 b	1.1589000	0.0000150	2459420.75780	0.00120	0.430	0.270	0.0620	0.0075	2.91	0.56	This Work	Esparza-Borges et al. (2022)
321669174	* TOI-2081 b	10.5053400	0.0000750	2458685.89960	0.00285	0.350	0.255	0.0396	0.0032	2.25	0.26	This Work	Esparza-Borges et al. (2022)
119584412	TOI-1801 b	10.6438700	0.0000550	2458903.54351	0.00328	0.265	0.180	0.0340	0.0010	2.03	0.08	This Work	Mallorquín et al. (2023)
166648874	TOI-1806.01	15.1454693	-	-	-	-	-	0.0778	-	3.33	-	This Work	Hord et al. (2024)
198385543	TOI-1846 b	3.9306737	0.0000043	2459565.95523	0.00031	0.464	0.051	0.0414	0.0007	1.87	0.06	This Work	Soubkion et al. (2025)
348755728	TOI-1883 b	4.5063800	0.0000065	2459256.84810	0.00020	0.210	0.145	0.0726	0.0029	5.76	0.28	This Work	Peláez-Torres et al. (2024)
368287008	TOI-2015 b	3.3482370	0.0000325	2459424.78570	0.00015	0.743	0.003	0.0928	0.0003	3.25	0.09	This Work	Jones et al. (2024)
417931300	* TOI-2068 b	7.7689150	0.0000310	2458683.42580	0.00265	0.460	0.280	0.0310	0.0020	1.83	0.13	This Work	Mistry et al. (2024)
59128183	TOI-2453 b	4.4414346	0.0000129	2459494.61240	0.00129	0.681	0.119	0.0590	0.0035	3.21	0.24	This Work	Lafarga et al. (2026)
16005254	TOI-5344 b	3.7926220	0.0000062	2459848.99030	0.00019	0.735	0.010	0.1653	0.0014	10.29	0.31	This Work	Hartman et al. (2023)
26054627	TOI-5349 b	3.3179210	0.0000020	2459521.81840	0.00050	0.510	0.040	0.1610	0.0020	10.00	0.31	This Work	Sandoval et al. (2026)
407591297	TOI-5388.01	2.5946748	0.0000036	2459348.07817	0.00053	0.430	0.285	0.0305	0.0014	1.06	0.07	This Work	Poultourizidis et al. (2026)
77156829	* LHS 1678 d	4.9652229	0.0000085	2459000.45806	0.00088	0.760	0.050	0.0273	0.0017	1.03	0.07	This Work	Silverstein et al. (2024)
219041246	TOI-5713 b	10.4419890	0.0000145	2458745.67760	0.00160	0.440	0.240	0.0541	0.0046	1.73	0.17	This Work	Ghachoui et al. (2024)
310380289	TOI-5736 b	0.6489900	0.0000100	2458738.89683	0.00149	0.435	0.194	0.0247	0.0007	1.56	0.06	This Work	Gomez Barrientos et al. (2026)
102734241	TOI-6002 b	10.9048210	0.0000195	2458692.76390	0.00260	0.260	0.175	0.0622	0.0075	1.65	0.22	This Work	Gomez Barrientos et al. (2026)
18318288	TOI-6086 b	1.3888725	0.0000827	2460131.96950	0.00057	0.608	0.051	0.0417	0.0022	1.18	0.07	This Work	Barkoui et al. (2024)
48353358	Kepler-1651 b	9.8786392	0.0000104	2454961.53395	0.00130	0.450	0.215	0.0336	0.0009	1.80	0.07	This Work	Mann et al. (2017)
368287008	TOI-2015 c	5.5827960	0.0000415	-	-	2.020	0.105	-	-	-	-	This Work	Barkoui et al. (2025)
441420236	AU Mic b	8.4634460	0.0000050	2458330.35088	0.00052	0.502	0.046	0.0499	0.0004	3.80	0.34	This Work	Mallorquín et al. (2024)
441420236	AU Mic c	18.8590230	0.0000230	2458342.22333	0.00110	0.259	0.191	0.0291	0.0004	2.21	0.20	This Work	Mallorquín et al. (2024)
388804061	K2-18 b	32.9396230	0.0000975	2457264.39144	0.00065	-	-	0.0529	0.0069	2.55	0.34	This Work	Sarkis et al. (2018)
38337202	K2-72 b	5.5772120	0.0004180	2457010.37600	0.00200	-	-	0.0299	0.0014	1.09	0.15	This Work	Dressing et al. (2017b)
38337202	K2-72 c	15.1890340	0.0031385	2456989.46500	0.00500	-	-	0.0323	0.0021	1.07	0.17	This Work	Dressing et al. (2017b)
38337202	K2-72 d	7.7601780	0.0014960	2456984.78800	0.00750	-	-	0.0279	0.0021	1.02	0.16	This Work	Dressing et al. (2017b)
38337202	K2-72 e	24.1588680	0.0037880	2456987.05400	0.00500	-	-	0.0358	0.0019	1.31	0.19	This Work	Dressing et al. (2017b)
27187450	Kepler-1652 b	38.0972200	0.0002100	2454973.00450	0.00470	0.011	0.122	0.0387	0.0017	1.70	0.31	This Work	Torres et al. (2017)
239275865	Kepler-560 b	18.4776445	0.0000152	2455018.26856	0.00061	-	-	0.0479	0.0007	2.15	0.16	This Work	Morton et al. (2016)

Table 5 continued

Table 5 (continued)

TIC	Planet Name	P_{orb} (d)	σ_P (d)	T_c (BJD)	σ_{T_c} (BJD)	b	σ_b	R_p/R_*	σ_{R_p/R_*}	R_p (R_{\oplus})	σ_{R_p} (R_{\oplus})	Stellar Reference	Planet Reference
268159861	Kepler-186 b	3.8867907	0.0000062	2454966.33040	0.00130	0.300	0.200	0.0208	0.0005	1.25	0.20	This Work	Quintana et al. (2014)
268159861	Kepler-186 e	22.4077040	0.0000730	2454986.80060	0.00240	0.310	0.200	0.0246	0.0006	1.49	0.24	This Work	Quintana et al. (2014)
268159861	Kepler-186 f	129.9441000	0.0012500	2455789.49400	0.00385	0.130	0.205	0.0205	0.0012	1.24	0.11	This Work	Torres et al. (2015)
268159861	Kepler-186 c	7.2673020	0.0000115	2455007.31420	0.00125	0.280	0.195	0.0242	0.0005	1.46	0.23	This Work	Quintana et al. (2014)
268159861	Kepler-186 d	13.3429960	0.0000245	2455009.90450	0.00145	0.360	0.215	0.0272	0.0007	1.64	0.26	This Work	Quintana et al. (2014)
273375582	Kepler-1229 b	86.8289890	0.0010690	2455022.26884	0.00777	-	-	0.0247	0.0016	1.55	0.15	This Work	Morton et al. (2016)
122450207	Kepler-1410 b	60.8661680	0.0005161	2455012.28498	0.00688	-	-	0.0274	0.0012	1.56	0.17	This Work	Morton et al. (2016)
158989438	Kepler-1512 b	20.3597260	0.0000587	2454967.29096	0.00240	-	-	0.0162	0.0006	0.59	0.10	This Work	Morton et al. (2016)
28090925	Kepler-1544 b	168.8111740	0.0012710	2455044.44085	0.00531	-	-	0.0220	0.0008	1.83	0.11	This Work	Morton et al. (2016)
120499135	Kepler-442 b	112.3053000	0.0026000	2455849.55780	0.00615	0.220	0.255	0.0211	0.0018	1.54	0.15	This Work	Torres et al. (2015)
173103335	K2-3 b	10.0546535	0.0000090	2457165.32947	0.00025	0.310	0.155	0.0349	0.0017	2.17	0.16	<i>a</i>	Diamond-Lowe et al. (2022)
150096001	* K2-133 b	3.0713300	0.0001100	2457821.31500	0.00155	0.630	0.053	0.0270	0.0020	1.39	0.13	<i>a</i>	Wells et al. (2019)
296739893	* TOI-620 b	5.0988179	0.0000046	2458992.19724	0.00073	0.887	0.015	0.0627	0.0032	3.69	0.21	<i>b</i>	Reefe et al. (2022)
144700903	TOI-532 b	2.3266508	0.0000030	2458470.57678	0.00088	-	-	0.0872	0.0034	5.79	0.28	<i>b</i>	Kanodia et al. (2021)
374180079	* K2-266 c	7.8140000	0.0017500	2457946.65100	0.00640	0.600	0.210	0.0092	0.0013	0.64	0.09	<i>a</i>	Rodríguez et al. (2018)
374339566	* K2-239 d	10.1150000	0.0010000	2457908.38100	-	0.390	0.250	0.0280	0.0027	0.83	0.17	<i>a</i>	Díez Alonso et al. (2018b)
82050863	* K2-9 b	18.4498000	0.0015000	2456822.67120	0.00290	0.926	0.250	0.0665	0.0283	2.69	1.18	<i>a</i>	Schlieder et al. (2016)
218795833	TOI-519 b	1.2652328	0.0000005	2458491.87712	-	-	-	0.3024	0.0123	11.58	0.58	<i>b</i>	Kagetani et al. (2023)
150096001	* K2-133 d	11.0245400	0.0003550	2457826.17090	0.00120	0.370	0.060	0.0404	0.0029	2.07	0.20	<i>a</i>	Wells et al. (2019)
283722336	HD 219134 d	46.8590000	0.0280000	2455208.44000	-	-	-	0.0190	0.0003	1.61	0.03	<i>d</i>	Gillon et al. (2017)
283722336	HD 219134 c	6.7645800	0.0003300	2457474.04591	0.00088	0.813	0.025	0.0178	0.0006	1.51	0.05	<i>d</i>	Gillon et al. (2017)
374180079	* K2-266 b	0.6585240	0.0000170	2457949.67470	0.00320	1.011	0.026	0.0430	0.0235	2.99	1.64	<i>a</i>	Rodríguez et al. (2018)
70899085	LP 714-47 b	4.0520370	0.0000040	2458774.70336	-	-	-	0.0738	0.0051	4.76	0.36	<i>b</i>	Dreizler et al. (2020)
408636441	TOI-1759 b	18.8501900	0.0001300	2458745.46540	0.00110	0.210	0.095	0.0482	0.0020	3.27	0.16	<i>b</i>	Espinoza et al. (2022)
374339566	* K2-239 c	7.7750000	0.0010000	2457916.86000	-	0.730	0.315	0.0255	0.0026	0.75	0.16	<i>a</i>	Díez Alonso et al. (2018b)
29960110	TOI-1201 b	2.4919863	0.0000031	2459169.23222	0.00053	0.404	0.076	0.0436	0.0021	2.29	0.13	<i>b</i>	Kossakowski et al. (2021)
243185500	TOI-1468 c	15.5324770	0.0000255	2458766.92670	0.00120	0.664	0.145	0.0525	0.0027	2.11	0.12	<i>b</i>	Meier Valdés et al. (2025a,b)
5882269	* K2-284 b	4.7950690	0.0000860	2457859.11316	0.00043	0.280	0.190	0.0420	0.0026	2.80	0.22	<i>a</i>	David et al. (2018)
150096001	* K2-133 e	26.5841000	0.0017500	2457837.86570	0.00225	0.928	0.047	0.0349	0.0033	1.79	0.20	<i>a</i>	Wells et al. (2019)
170849515	HATS-76 b	1.9416423	0.0000014	2458424.55556	0.00053	0.281	0.092	0.1772	0.0056	12.48	0.55	<i>b</i>	Jordán et al. (2022b)
83181153	* K2-26 b	14.5665000	0.0018000	2456775.16590	0.00245	0.570	0.315	0.0471	0.0109	2.68	0.64	<i>a</i>	Schlieder et al. (2016)
173103335	K2-3 d	44.5560300	0.0001250	2457271.78796	0.00076	0.240	0.160	0.0245	0.0012	1.52	0.11	<i>a</i>	Diamond-Lowe et al. (2022)
437054764	K2-419 A b	20.3584725	0.0000059	2459553.71380	0.00050	0.389	0.089	0.1788	0.0087	10.67	0.77	<i>c</i>	Kanodia et al. (2024)
283722336	HD 219134 f	22.7170000	0.0150000	2455233.17000	-	-	-	0.0154	0.0003	1.31	0.02	<i>d</i>	Gillon et al. (2017)
28900646	TOI-1685 b	0.6691392	0.0000004	2459910.93828	0.00040	0.266	0.069	0.0295	0.0013	1.48	0.08	<i>b</i>	Burt et al. (2024)
283722336	HD 219134 b	3.0929260	0.0000100	2457126.69913	0.00087	0.924	0.006	0.0189	0.0007	1.60	0.06	<i>d</i>	Gillon et al. (2017)
203214081	G 9-40 b	5.7459982	0.0000020	2459503.32682	0.00042	0.513	0.042	0.0576	0.0027	1.99	0.11	<i>b</i>	Luque et al. (2022b)
389900760	* TOI-2120 b	5.7998164	0.0000035	2458795.82368	0.00041	0.550	0.085	0.0794	0.0031	2.08	0.10	<i>b</i>	Hori et al. (2024)
423358488	* K2-148 b	4.3839500	0.0008000	2457390.05956	0.00961	-	-	0.0193	0.0034	1.29	0.24	<i>a</i>	Hirano et al. (2018)

Table 5 continued

Table 5 (continued)

TIC	Planet Name	P_{orb} (d)	σ_P (d)	T_c (BJD)	σ_{T_c} (BJD)	b	σ_b	R_p/R_*	σ_{R_p/R_*}	R_p (R_\oplus)	σ_{R_p} (R_\oplus)	Stellar Reference	Planet Reference
18310799	K2-136 c	17.3071300	0.0002700	2457812.71770	0.00085	0.310	0.125	0.0406	0.0024	2.72	0.20	<i>a</i>	Mayo et al. (2023)
423358488	* K2-148 d	9.7579000	0.0010000	2457386.34305	0.00545	-	-	0.0238	0.0042	1.60	0.29	<i>a</i>	Hirano et al. (2018)
374180079	* K2-266 e	19.4820000	0.0012000	2457938.54100	0.00130	0.360	0.130	0.0356	0.0022	2.47	0.18	<i>a</i>	Rodríguez et al. (2018)
374180079	* K2-266 d	14.6970000	0.0003450	2457944.83930	0.00120	0.290	0.145	0.0382	0.0022	2.65	0.19	<i>a</i>	Rodríguez et al. (2018)
173103335	K2-3 c	24.6467290	0.0000430	2457329.85688	0.00055	0.140	0.115	0.0266	0.0013	1.65	0.12	<i>a</i>	Diamond-Lowe et al. (2022)
18310799	K2-136 d	25.5750000	0.0023500	2457780.81170	0.00650	0.677	0.045	0.0212	0.0013	1.42	0.11	<i>a</i>	Mayo et al. (2023)
470381900	TOI-1696 b	2.5003110	0.0000040	2458834.20115	0.00058	0.590	0.035	0.1021	0.0047	3.07	0.17	<i>b</i>	Mori et al. (2022)
343628284	* TOI-1448 b	8.1122450	0.0000180	2458713.33750	0.00150	0.210	0.150	0.0663	0.0020	2.74	0.12	<i>b</i>	Hori et al. (2024)
163539739	TOI-1278 b	14.4756700	0.0002100	2458711.95950	0.00130	1.040	0.055	0.1955	0.0432	11.79	2.63	<i>b</i>	Artigau et al. (2021b)
118327550	TOI-244 b	7.3972250	0.0000245	2458357.36270	0.00200	0.610	0.310	0.0327	0.0032	1.46	0.15	<i>b</i>	Castro-González et al. (2023)
212957629	* TOI-2406 b	3.0766891	0.0000024	2459115.97600	0.00030	0.090	0.075	0.1285	0.0038	2.85	0.12	<i>b</i>	Hori et al. (2024)
18310799	K2-136 b	7.9752000	0.0007900	2457817.75630	0.00470	0.220	0.145	0.0137	0.0009	0.92	0.07	<i>a</i>	Mayo et al. (2023)
243185500	TOI-1468 b	1.8805201	0.0000027	2458765.67755	0.00089	0.465	0.071	0.0346	0.0017	1.39	0.08	<i>b</i>	Meier Valdés et al. (2025a,b)
150096001	K2-133 c	4.8678400	0.0001200	2457823.76860	0.00110	0.640	0.046	0.0323	0.0024	1.66	0.16	<i>a</i>	Wells et al. (2019)
423358488	* K2-148 c	6.9226000	0.0007000	2457387.72777	0.00458	-	-	0.0251	0.0043	1.68	0.30	<i>a</i>	Hirano et al. (2018)
374339566	* K2-239 b	5.2400000	0.0010000	2457908.19100	-	0.440	0.310	0.0280	0.0027	0.83	0.17	<i>a</i>	Díez Alonso et al. (2018b)
301289516	GJ 9827 d	6.2018300	0.0000030	2460265.10196	0.00006	0.891	0.009	0.0313	0.0024	2.23	0.26	<i>a</i>	Piaulet-Ghorayeb et al. (2024)
452866790	GJ 3473 b	1.1980035	0.0000019	2458492.20408	0.00043	0.336	0.070	0.0318	0.0016	1.24	0.07	<i>b</i>	Kemmer et al. (2020)
387690507	TOI-530 b	6.3875970	0.0000185	2458470.19980	0.00165	0.330	0.095	0.1580	0.0144	9.15	0.87	<i>b</i>	Gan et al. (2022)

Planet parameters for confirmed and validated (denoted with an asterisk in the Planet Name column) planets. Missing parameters that were not reported in the corresponding paper cited in the Planet Source column are denoted with a “-”. Planet orbital period (P), time of conjunction (t_c), impact parameter (b) and planet-to-star radius ratio (R_p/R_*) were taken from the publications cited in the Planet Reference column. **The updated planet radii (R_p) were calculated using the stellar radii reported in Table 4 in this work, Dressing et al. (2017a), Dressing et al. (2019), Mann et al. (2013c), and Gore et al. (2024).** ^aDressing et al. (2019) ^bGore et al. (2024) ^cDressing et al. (2017a) ^dMann et al. (2013c)

Table 6. Updated planet parameters for planet candidates in our sample, using stellar parameters reported in Table 4

TIC	TOI	P_{orb} (d)	σ_P (d)	T_c (BJD)	σ_{T_c} (BJD)	b	σ_b	R_p/R_*	σ_{R_p/R_*}	R_p (R_{\oplus})	σ_{R_p} (R_{\oplus})
415969908	233.01	11.6700370	0.0000120	2458365.2606	0.0020	0.803	0.019	0.051	0.003	2.12	0.13
415969908	233.02	7.2011660	0.0000240	2458359.4715	0.0060	0.598	0.073	0.036	0.003	1.51	0.15
312862941	1638.01	0.9150623	0.0000006	2459908.4409	0.0004	1.014	0.007	0.095	0.005	7.21	0.33
232635922	1745.01	5.9848710	0.0000133	2459653.4738	0.0013	0.829	0.037	0.051	0.003	2.44	0.16
332477926	1754.01	16.2143217	0.0000468	2459662.8087	0.0018	0.564	0.060	0.036	0.002	2.36	0.11
138762614	1802.01	16.7961107	0.0193909	2458904.1494	0.0078	0.426	0.208	0.034	0.004	2.18	0.24
166648874	1806.02	8.1960758	0.0000542	2458905.2286	0.0038	1.019	0.095	0.157	0.076	6.72	3.93
166648874	1806.03	0.5019031	0.0000023	2458899.7005	0.0026	0.863	0.049	0.040	0.005	1.73	0.30
321669174	2081.02	5.1097197	0.0000215	2458686.9747	0.0057	0.873	0.037	0.026	0.002	1.45	0.12
243313296	2278.01	1.4663344	0.0000012	2459690.5881	0.0005	0.925	0.007	0.034	0.002	1.21	0.10
405763009 ^a	2433.01	-	-	2458746.3710	0.0243	1.089	0.099	0.172	0.083	5.83	2.84
59128183	2453.01	4.4414275	0.0000080	2458441.9926	0.0020	0.885	0.045	0.068	0.005	3.68	0.29
202185707	4325.01	1.6500673	0.0000009	2458469.3689	0.0007	0.906	0.048	0.074	0.006	3.63	0.35
337385330	5112.01	15.5328060	0.0000730	2460261.2915	0.0028	0.678	0.081	0.027	0.002	1.78	0.09
389040826	5511.01	4.7174703	0.0159134	2459575.0454	0.0499	0.909	0.130	0.130	0.096	7.24	6.75
443582629	5519.01	5.8512587	0.0000531	2459284.3922	0.0042	0.542	0.130	0.035	0.003	1.39	0.14
387974148	5551.01	2.4054100	0.0000331	2459474.7182	0.0035	0.604	0.143	0.030	0.003	1.78	0.18
422217860	5662.01	2.3144207	0.0000049	2459689.6707	0.0013	0.786	0.041	0.045	0.002	2.98	0.16
310380289	5736.01	0.6489868	0.0000019	2458738.8948	0.0029	0.764	0.112	0.025	0.003	1.55	0.14
434116397	5955.01	0.5902387	0.0000017	2459825.8482	0.0015	0.776	0.051	0.022	0.001	1.39	0.08
262689575	5961.01	1.6174870	0.0000049	2459447.7808	0.0025	0.738	0.069	0.010	0.001	0.64	0.06
354173595	5974.01	1.7266943	0.0000026	2459447.8998	0.0014	0.874	0.026	0.036	0.002	1.49	0.08
120045750	5981.01	7.0142458	0.0000310	2459423.5177	0.0022	0.645	0.084	0.039	0.002	2.31	0.12
284900292	5987.01	48.7130843	0.0003269	2458769.9812	0.0092	0.751	0.069	0.039	0.003	2.63	0.19
196066560	6077.01	2.2111104	0.0004362	2458713.4706	0.0181	0.269	0.198	0.023	0.003	1.64	0.24

^aTESS has only observed two transits of TOI 2433.01. We therefore do not report an orbital period for this planet candidate, and define the time of conjunction (T_c) as the midpoint of the first observed transit.

C. THEORETICAL RADIUS VALLEY SCALINGS

As well as the empirical relations for the radius valley shown in Fig. 5 and used to generate the super-Earth and sub-Neptune stellar metallicity cumulative distribution functions (CDFs) shown in Fig. 6, we also considered theoretical radius valley scalings. Firstly, we used the scaling presented in Lopez & Rice (2018) which was derived assuming photo-evaporative mass-loss due to stellar irradiation. Secondly, we considered a radius valley sculpted by core-powered mass-loss (Gupta & Schlichting 2019). Finally, we considered the results of super-Earth formation in a gas-depleted disk, as presented in Lopez & Rice (2018). Similarly to Fig. 6, we calculated stellar metallicity CDFs for the super-Earth and sub-Neptune planet hosts, as shown in Fig. C.

We find that the super-Earth and sub-Neptune metallicity samples are inconsistent with being drawn from the same underlying distribution under the gas-depleted formation scaling. Under the photo-evaporative and core-powered mass-loss scenarios, we cannot reject the null hypothesis that the stellar metallicity distributions for super-Earth and sub-Neptune hosts are drawn from the same distribution.

Cloutier & Menou (2020) found that the radius valley around early to mid M dwarfs is most consistent with the gas-depleted scenario in radius-instellation space. Therefore, we argue that the results for the gas-depleted formation radius valley scaling are most appropriate to interpret for our sample, and that these results are in line with the empirical radius valley scaling results discussed in Section 6.

REFERENCES

- NASA Exoplanet Archive . 2019, Confirmed Planets Table, IPAC, doi: [10.26133/NEA12](https://doi.org/10.26133/NEA12)
- Abbott, T. M. C., Walker, A. R., Points, S. D., et al. 2016, in Society of Photo-Optical Instrumentation Engineers (SPIE) Conference Series, Vol. 9906, Ground-based and Airborne Telescopes VI, ed. H. J. Hall, R. Gilmozzi, & H. K. Marshall, 99064D, doi: [10.1117/12.2232723](https://doi.org/10.1117/12.2232723)
- Agol, E., Luger, R., & Foreman-Mackey, D. 2020, AJ, 159, 123, doi: [10.3847/1538-3881/ab4fee](https://doi.org/10.3847/1538-3881/ab4fee)
- Alessi, M., Inglis, J., & Pudritz, R. E. 2020, MNRAS, 497, 4814, doi: [10.1093/mnras/staa2087](https://doi.org/10.1093/mnras/staa2087)
- Antoniadis-Karnavas, A., Sousa, S. G., Delgado-Mena, E., Santos, N. C., & Andreasen, D. T. 2024, A&A, 690, A58, doi: [10.1051/0004-6361/202450722](https://doi.org/10.1051/0004-6361/202450722)
- Artigau, É., Hébrard, G., Cadieux, C., et al. 2021a, AJ, 162, 144, doi: [10.3847/1538-3881/ac096d](https://doi.org/10.3847/1538-3881/ac096d)
- . 2021b, AJ, 162, 144, doi: [10.3847/1538-3881/ac096d](https://doi.org/10.3847/1538-3881/ac096d)
- Astropy Collaboration, Robitaille, T. P., Tollerud, E. J., et al. 2013, A&A, 558, A33, doi: [10.1051/0004-6361/201322068](https://doi.org/10.1051/0004-6361/201322068)
- Astropy Collaboration, Price-Whelan, A. M., Sipőcz, B. M., et al. 2018, AJ, 156, 123, doi: [10.3847/1538-3881/aabc4f](https://doi.org/10.3847/1538-3881/aabc4f)
- Astropy Collaboration, Price-Whelan, A. M., Lim, P. L., et al. 2022, ApJ, 935, 167, doi: [10.3847/1538-4357/ac7c74](https://doi.org/10.3847/1538-4357/ac7c74)
- Barkaoui, K., Schwarz, R. P., Narita, N., et al. 2024, A&A, 687, A264, doi: [10.1051/0004-6361/202349127](https://doi.org/10.1051/0004-6361/202349127)
- Barkaoui, K., Korth, J., Gaidos, E., et al. 2025, A&A, 695, A281, doi: [10.1051/0004-6361/202452916](https://doi.org/10.1051/0004-6361/202452916)
- Bean, J. L., Benedict, G. F., & Endl, M. 2006, ApJL, 653, L65, doi: [10.1086/510527](https://doi.org/10.1086/510527)
- Bean, J. L., Raymond, S. N., & Owen, J. E. 2021, JGRE, 126, e06639, doi: [10.1029/2020JE006639](https://doi.org/10.1029/2020JE006639)
- Behrard, A., Ness, M. K., Casey, A. R., et al. 2025, ApJ, 982, 13, doi: [10.3847/1538-4357/adaf1f](https://doi.org/10.3847/1538-4357/adaf1f)
- Beleznyay, M., & Kunimoto, M. 2022, MNRAS, 516, 75, doi: [10.1093/mnras/stac2179](https://doi.org/10.1093/mnras/stac2179)
- Bitsch, B., & Johansen, A. 2016, A&A, 590, A101, doi: [10.1051/0004-6361/201527676](https://doi.org/10.1051/0004-6361/201527676)
- Bitsch, B., Raymond, S. N., & Izidoro, A. 2019, A&A, 624, A109, doi: [10.1051/0004-6361/201935007](https://doi.org/10.1051/0004-6361/201935007)
- Boley, K. M., Christiansen, J. L., Zink, J., et al. 2024, AJ, 168, 128, doi: [10.3847/1538-3881/ad6570](https://doi.org/10.3847/1538-3881/ad6570)
- Bonfils, X., Delfosse, X., Udry, S., et al. 2005, A&A, 442, 635, doi: [10.1051/0004-6361:20053046](https://doi.org/10.1051/0004-6361:20053046)
- Boss, A. P. 1997, Science, 276, 1836, doi: [10.1126/science.276.5320.1836](https://doi.org/10.1126/science.276.5320.1836)
- Bowler, B. P., Blunt, S. C., & Nielsen, E. L. 2020, AJ, 159, 63, doi: [10.3847/1538-3881/ab5b11](https://doi.org/10.3847/1538-3881/ab5b11)
- Brugger, B., Mousis, O., Deleuil, M., & Deschamps, F. 2017, ApJ, 850, 93, doi: [10.3847/1538-4357/aa965a](https://doi.org/10.3847/1538-4357/aa965a)
- Bryan, M. L., & Lee, E. J. 2025, ApJL, 982, L7, doi: [10.3847/2041-8213/adb0bd](https://doi.org/10.3847/2041-8213/adb0bd)
- Bryant, E. M., Bayliss, D., & Van Eylen, V. 2023, MNRAS, 521, 3663, doi: [10.1093/mnras/stad626](https://doi.org/10.1093/mnras/stad626)
- Buchhave, L. A., Latham, D. W., Johansen, A., et al. 2012, Nature, 486, 375, doi: [10.1038/nature11121](https://doi.org/10.1038/nature11121)
- Burn, R., Mordasini, C., Mishra, L., et al. 2024, NatAs, 8, 463, doi: [10.1038/s41550-023-02183-7](https://doi.org/10.1038/s41550-023-02183-7)
- Burn, R., Schlecker, M., Mordasini, C., et al. 2021, A&A, 656, A72, doi: [10.1051/0004-6361/202140390](https://doi.org/10.1051/0004-6361/202140390)
- Burt, J. A., Hooton, M. J., Mamajek, E. E., et al. 2024, ApJL, 971, L12, doi: [10.3847/2041-8213/ad5b52](https://doi.org/10.3847/2041-8213/ad5b52)

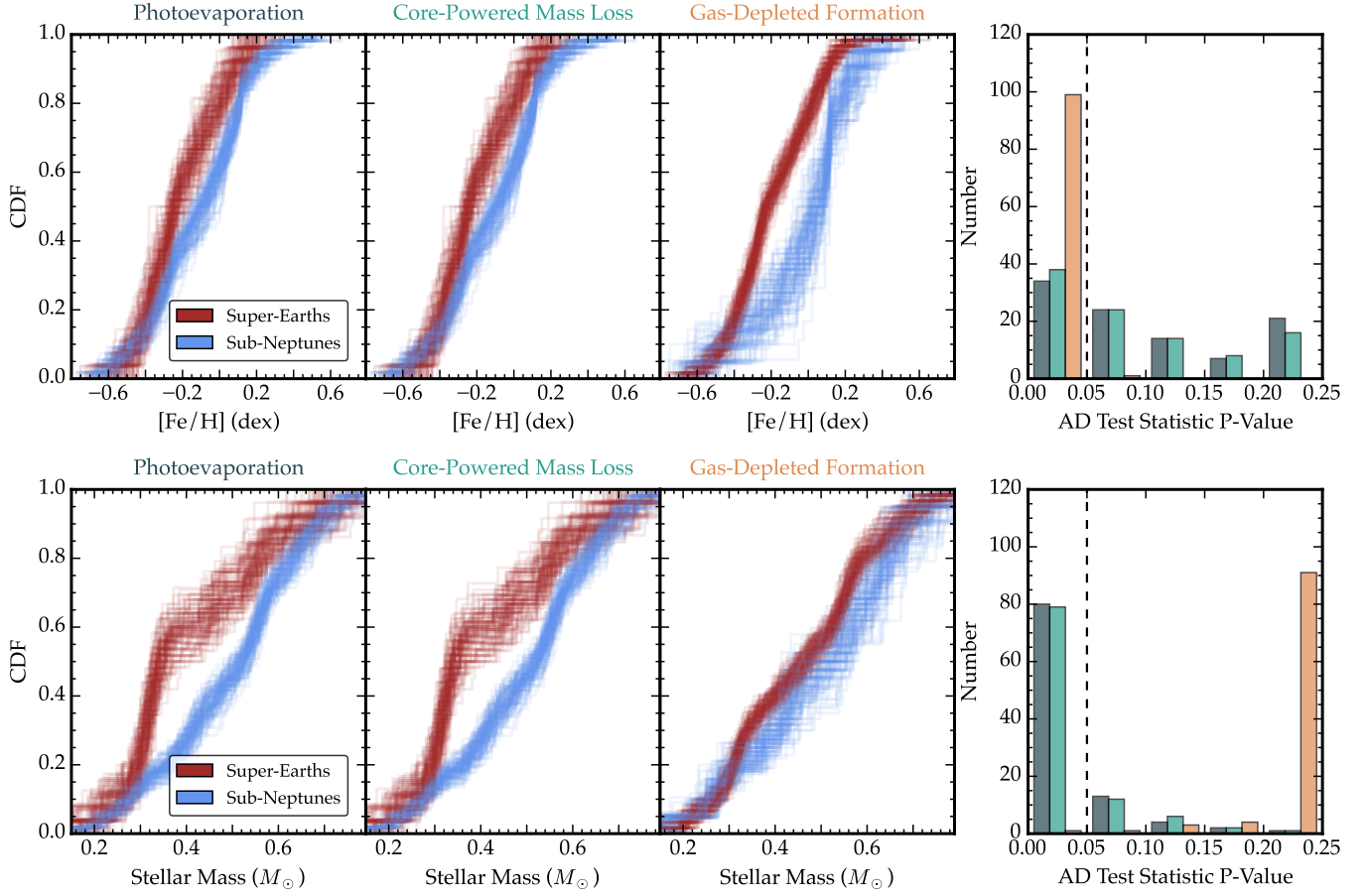


Figure 8. (Left 3 plots:) Cumulative distribution function of measured metallicities (top row) and stellar mass (bottom row) for super-Earths (brown) and sub-Neptunes (blue). The distinction between the two populations are set following the radius valley prescriptions for the photoevaporation (navy), core-powered mass loss (teal), and gas-depleted formation (yellow) scenarios. (Right:) Histograms showing the p-values associated with the k-sample Anderson-Darling (AD) (Scholz & Stephens 1987) tests for the stellar metallicity (top) and mass (bottom) distributions for each of 100 draws from the planet sample plotted in Fig. 5. A vertical dashed black line at a p-value of 0.05 indicates a typical upper threshold used to reject the null hypothesis under an AD test. The null hypothesis is that the sub-Neptune and super-Earth host stellar metallicity samples are drawn from the same underlying distribution. This null hypothesis is most inconsistent with the observed stellar metallicity distributions using the gas-depleted formation prescription for the radius valley.

- Casey, A. R., Hogg, D. W., Ness, M., et al. 2016, arXiv e-prints, arXiv:1603.03040, doi: [10.48550/arXiv.1603.03040](https://doi.org/10.48550/arXiv.1603.03040)
- Castro González, A., Díez Alonso, E., Menéndez Blanco, J., et al. 2020, MNRAS, 499, 5416, doi: [10.1093/mnras/staa2353](https://doi.org/10.1093/mnras/staa2353)
- Castro-González, A., Demangeon, O. D. S., Lillo-Box, J., et al. 2023, A&A, 675, A52, doi: [10.1051/0004-6361/202346550](https://doi.org/10.1051/0004-6361/202346550)
- Chabrier, G., Johansen, A., Janson, M., & Rafikov, R. 2014, in Protostars and Planets VI, ed. H. Beuther, R. S. Klessen, C. P. Dullemond, & T. Henning, 619–642, doi: [10.2458/azu_uapress.9780816531240-ch027](https://doi.org/10.2458/azu_uapress.9780816531240-ch027)
- Chachan, Y., Fortney, J. J., Ohno, K., Thorngren, D., & Murray-Clay, R. 2025, ApJ, 994, 43, doi: [10.3847/1538-4357/ae0cbf](https://doi.org/10.3847/1538-4357/ae0cbf)
- Chen, H., Clement, M. S., Wang, L. C., & Gu, J. T. 2025, ApJL, 991, L11, doi: [10.3847/2041-8213/adf282](https://doi.org/10.3847/2041-8213/adf282)
- Cherubim, C., Cloutier, R., Charbonneau, D., et al. 2023, AJ, 165, 167, doi: [10.3847/1538-3881/acbdfd](https://doi.org/10.3847/1538-3881/acbdfd)
- Chiang, E., & Laughlin, G. 2013, MNRAS, 431, 3444, doi: [10.1093/mnras/stt424](https://doi.org/10.1093/mnras/stt424)
- Chittidi, J. S., Muirhead, P. S., Rojas-Ayala, B., & Jorgenson, R. A. 2019, in American Astronomical Society Meeting Abstracts, Vol. 233, American Astronomical Society Meeting Abstracts #233, 140.01
- Cloutier, R., & Menou, K. 2020, AJ, 159, 211, doi: [10.3847/1538-3881/ab8237](https://doi.org/10.3847/1538-3881/ab8237)
- Cosentino, R., Lovis, C., Pepe, F., et al. 2012, in Society of Photo-Optical Instrumentation Engineers (SPIE) Conference Series, Vol. 8446, Ground-based and Airborne Instrumentation for Astronomy IV, ed. I. S. McLean, S. K. Ramsay, & H. Takami, 84461V, doi: [10.1117/12.925738](https://doi.org/10.1117/12.925738)
- Cushing, M. C., Vacca, W. D., & Rayner, J. T. 2004, PASP, 116, 362, doi: [10.1086/382907](https://doi.org/10.1086/382907)
- David, T. J., Mamajek, E. E., Vanderburg, A., et al. 2018, AJ, 156, 302, doi: [10.3847/1538-3881/aaed7](https://doi.org/10.3847/1538-3881/aaed7)
- Dawson, R. I., Chiang, E., & Lee, E. J. 2015, MNRAS, 453, 1471, doi: [10.1093/mnras/stv1639](https://doi.org/10.1093/mnras/stv1639)
- de Leon, J. P., Livingston, J., Endl, M., et al. 2021, MNRAS, 508, 195, doi: [10.1093/mnras/stab2305](https://doi.org/10.1093/mnras/stab2305)
- Diamond-Lowe, H., Kreidberg, L., Harman, C. E., et al. 2022, AJ, 164, 172, doi: [10.3847/1538-3881/ac7807](https://doi.org/10.3847/1538-3881/ac7807)
- Díez Alonso, E., Suárez Gómez, S. L., González Hernández, J. I., et al. 2018a, MNRAS, 476, L50, doi: [10.1093/mnrasl/sly040](https://doi.org/10.1093/mnrasl/sly040)
- Díez Alonso, E., González Hernández, J. I., Suárez Gómez, S. L., et al. 2018b, MNRAS, 480, L1, doi: [10.1093/mnrasl/sly102](https://doi.org/10.1093/mnrasl/sly102)
- Donati, J.-F., Kouach, D., Moutou, C., et al. 2020, MNRAS, 498, 5684, doi: [10.1093/mnras/staa2569](https://doi.org/10.1093/mnras/staa2569)
- Dreizler, S., Crossfield, I. J. M., Kossakowski, D., et al. 2020, A&A, 644, A127, doi: [10.1051/0004-6361/202038016](https://doi.org/10.1051/0004-6361/202038016)
- Dressing, C. D., & Charbonneau, D. 2013, ApJ, 767, 95, doi: [10.1088/0004-637X/767/1/95](https://doi.org/10.1088/0004-637X/767/1/95)
- Dressing, C. D., Newton, E. R., Schlieder, J. E., et al. 2017a, ApJ, 836, 167, doi: [10.3847/1538-4357/836/2/167](https://doi.org/10.3847/1538-4357/836/2/167)
- Dressing, C. D., Vanderburg, A., Schlieder, J. E., et al. 2017b, AJ, 154, 207, doi: [10.3847/1538-3881/aa89f2](https://doi.org/10.3847/1538-3881/aa89f2)
- Dressing, C. D., Hardegree-Ullman, K., Schlieder, J. E., et al. 2019, AJ, 158, 87, doi: [10.3847/1538-3881/ab2895](https://doi.org/10.3847/1538-3881/ab2895)
- Duque-Arribas, C., Montes, D., Tabernero, H. M., et al. 2023, ApJ, 944, 106, doi: [10.3847/1538-4357/acac6f](https://doi.org/10.3847/1538-4357/acac6f)
- Eastman, J. D., Rodriguez, J. E., Agol, E., et al. 2019, arXiv e-prints, arXiv:1907.09480, doi: [10.48550/arXiv.1907.09480](https://doi.org/10.48550/arXiv.1907.09480)
- Emsenhuber, A., Mordasini, C., Burn, R., et al. 2021, A&A, 656, A69, doi: [10.1051/0004-6361/202038553](https://doi.org/10.1051/0004-6361/202038553)
- Endl, M., & Cochran, W. D. 2016, PASP, 128, 094502, doi: [10.1088/1538-3873/128/967/094502](https://doi.org/10.1088/1538-3873/128/967/094502)
- Esparza-Borges, E., Parviainen, H., Murgas, F., et al. 2022, A&A, 666, A10, doi: [10.1051/0004-6361/202243731](https://doi.org/10.1051/0004-6361/202243731)
- Espinoza, N., Pallé, E., Kemmer, J., et al. 2022, AJ, 163, 133, doi: [10.3847/1538-3881/ac4af0](https://doi.org/10.3847/1538-3881/ac4af0)
- ExoFOP. 2019, Exoplanet Follow-up Observing Program - TESS, IPAC, doi: [10.26134/ExoFOP3](https://doi.org/10.26134/ExoFOP3)
- Fischer, D. A., & Valenti, J. 2005, ApJ, 622, 1102, doi: [10.1086/428383](https://doi.org/10.1086/428383)
- Foreman-Mackey, D., Luger, R., Agol, E., et al. 2021, arXiv e-prints, arXiv:2105.01994, <https://arxiv.org/abs/2105.01994>
- Foreman-Mackey, D., Savel, A., Luger, R., et al. 2021, exoplanet-dev/exoplanet v0.5.1, doi: [10.5281/zenodo.1998447](https://doi.org/10.5281/zenodo.1998447)
- Fulton, B. J., Petigura, E. A., Howard, A. W., et al. 2017, AJ, 154, 109, doi: [10.3847/1538-3881/aa80eb](https://doi.org/10.3847/1538-3881/aa80eb)
- Gaidos, E. 2017, MNRAS, 470, L1, doi: [10.1093/mnrasl/slx063](https://doi.org/10.1093/mnrasl/slx063)
- Gan, T., Theissen, C. A., Wang, S. X., Burgasser, A. J., & Mao, S. 2025, ApJS, 276, 47, doi: [10.3847/1538-4365/ad9c65](https://doi.org/10.3847/1538-4365/ad9c65)
- Gan, T., Lin, Z., Wang, S. X., et al. 2022, MNRAS, 511, 83, doi: [10.1093/mnras/stab3708](https://doi.org/10.1093/mnras/stab3708)
- Ghachoui, M., Rackham, B. V., Dévora-Pajares, M., et al. 2024, A&A, 690, A263, doi: [10.1051/0004-6361/202451120](https://doi.org/10.1051/0004-6361/202451120)
- Ghezzi, L., Montet, B. T., & Johnson, J. A. 2018, ApJ, 860, 109, doi: [10.3847/1538-4357/aac37c](https://doi.org/10.3847/1538-4357/aac37c)

- Giacalone, S., Dressing, C. D., Jensen, E. L. N., et al. 2021, *AJ*, 161, 24, doi: [10.3847/1538-3881/abc6af](https://doi.org/10.3847/1538-3881/abc6af)
- Gillis, E., Cloutier, R., & Pass, E. 2026, arXiv e-prints, arXiv:2602.23364, doi: [10.48550/arXiv.2602.23364](https://doi.org/10.48550/arXiv.2602.23364)
- Gillon, M., Demory, B.-O., Van Grootel, V., et al. 2017, *NatAs*, 1, 0056, doi: [10.1038/s41550-017-0056](https://doi.org/10.1038/s41550-017-0056)
- Ginsburg, A., Sipőcz, B. M., Brasseur, C. E., et al. 2019, *AJ*, 157, 98, doi: [10.3847/1538-3881/aafc33](https://doi.org/10.3847/1538-3881/aafc33)
- Gomez Barrientos, J., Knutson, H. A., Saidel, M., et al. 2026, *AJ*, 171, 99, doi: [10.3847/1538-3881/ae246f](https://doi.org/10.3847/1538-3881/ae246f)
- Gore, R., Giacalone, S., Dressing, C. D., et al. 2024, *ApJS*, 271, 48, doi: [10.3847/1538-4365/ad2c0c](https://doi.org/10.3847/1538-4365/ad2c0c)
- Gunn, J. E., Siegmund, W. A., Mannery, E. J., et al. 2006, *AJ*, 131, 2332, doi: [10.1086/500975](https://doi.org/10.1086/500975)
- Gupta, A., Nicholson, L., & Schlichting, H. E. 2022, *MNRAS*, 516, 4585, doi: [10.1093/mnras/stac2488](https://doi.org/10.1093/mnras/stac2488)
- Gupta, A., & Schlichting, H. E. 2019, *MNRAS*, 487, 24, doi: [10.1093/mnras/stz1230](https://doi.org/10.1093/mnras/stz1230)
- . 2020, *MNRAS*, 493, 792, doi: [10.1093/mnras/staa315](https://doi.org/10.1093/mnras/staa315)
- Hardegree-Ullman, K. K., Cushing, M. C., Muirhead, P. S., & Christiansen, J. L. 2019, *AJ*, 158, 75, doi: [10.3847/1538-3881/ab21d2](https://doi.org/10.3847/1538-3881/ab21d2)
- Harris, C. R., Millman, K. J., van der Walt, S. J., et al. 2020, *Nature*, 585, 357, doi: [10.1038/s41586-020-2649-2](https://doi.org/10.1038/s41586-020-2649-2)
- Hartman, J. D., Bakos, G. Á., Csabry, Z., et al. 2023, *AJ*, 166, 163, doi: [10.3847/1538-3881/acf56e](https://doi.org/10.3847/1538-3881/acf56e)
- Hejazi, N., De Robertis, M. M., & Dawson, P. C. 2015, *AJ*, 149, 140, doi: [10.1088/0004-6256/149/4/140](https://doi.org/10.1088/0004-6256/149/4/140)
- Henry, T. J., & Jao, W.-C. 2024, *ARA&A*, 62, 593, doi: [10.1146/annurev-astro-052722-102740](https://doi.org/10.1146/annurev-astro-052722-102740)
- Hirano, T., Dai, F., Livingston, J. H., et al. 2018, *AJ*, 155, 124, doi: [10.3847/1538-3881/aaaa6e](https://doi.org/10.3847/1538-3881/aaaa6e)
- Ho, C. S. K., Rogers, J. G., Van Eylen, V., Owen, J. E., & Schlichting, H. E. 2024, *MNRAS*, 531, 3698, doi: [10.1093/mnras/stae1376](https://doi.org/10.1093/mnras/stae1376)
- Hoffman, M. D., & Gelman, A. 2011, arXiv e-prints, arXiv:1111.4246, doi: [10.48550/arXiv.1111.4246](https://doi.org/10.48550/arXiv.1111.4246)
- Hord, B. J., Kempton, E. M.-R., Evans-Soma, T. M., et al. 2024, *AJ*, 167, 233, doi: [10.3847/1538-3881/ad3068](https://doi.org/10.3847/1538-3881/ad3068)
- Hori, Y., Fukui, A., Hirano, T., et al. 2024, *AJ*, 167, 289, doi: [10.3847/1538-3881/ad4115](https://doi.org/10.3847/1538-3881/ad4115)
- Howard, A. W., Marcy, G. W., Bryson, S. T., et al. 2012, *ApJS*, 201, 15, doi: [10.1088/0067-0049/201/2/15](https://doi.org/10.1088/0067-0049/201/2/15)
- Hunter, J. D. 2007, *Computing in Science & Engineering*, 9, 90, doi: [10.1109/MCSE.2007.55](https://doi.org/10.1109/MCSE.2007.55)
- Ida, S., & Lin, D. N. C. 2004, *ApJ*, 616, 567, doi: [10.1086/424830](https://doi.org/10.1086/424830)
- Jenkins, J. M., Twicken, J. D., McCauliff, S., et al. 2016, in *Society of Photo-Optical Instrumentation Engineers (SPIE) Conference Series*, Vol. 9913, Software and Cyberinfrastructure for Astronomy IV, ed. G. Chiozzi & J. C. Guzman, 99133E, doi: [10.1117/12.2233418](https://doi.org/10.1117/12.2233418)
- Jofré, P., Heiter, U., & Soubiran, C. 2019, *ARA&A*, 57, 571, doi: [10.1146/annurev-astro-091918-104509](https://doi.org/10.1146/annurev-astro-091918-104509)
- Johansen, A., & Lambrechts, M. 2017, *AREPS*, 45, 359, doi: [10.1146/annurev-earth-063016-020226](https://doi.org/10.1146/annurev-earth-063016-020226)
- Johnson, J. A., & Apps, K. 2009, *ApJ*, 699, 933, doi: [10.1088/0004-637X/699/2/933](https://doi.org/10.1088/0004-637X/699/2/933)
- Jones, S. E., Stefánsson, G., Masuda, K., et al. 2024, *AJ*, 168, 93, doi: [10.3847/1538-3881/ad55ea](https://doi.org/10.3847/1538-3881/ad55ea)
- Jordán, A., Hartman, J. D., Bayliss, D., et al. 2022a, *AJ*, 163, 125, doi: [10.3847/1538-3881/ac4a77](https://doi.org/10.3847/1538-3881/ac4a77)
- . 2022b, *AJ*, 163, 125, doi: [10.3847/1538-3881/ac4a77](https://doi.org/10.3847/1538-3881/ac4a77)
- Kagetani, T., Narita, N., Kimura, T., et al. 2023, *PASJ*, 75, 713, doi: [10.1093/pasj/psad031](https://doi.org/10.1093/pasj/psad031)
- Kanodia, S., Stefansson, G., Cañas, C. I., et al. 2021, *AJ*, 162, 135, doi: [10.3847/1538-3881/ac1940](https://doi.org/10.3847/1538-3881/ac1940)
- Kanodia, S., Gupta, A. F., Cañas, C. I., et al. 2024, *AJ*, 168, 235, doi: [10.3847/1538-3881/ad7796](https://doi.org/10.3847/1538-3881/ad7796)
- Kemmer, J., Stock, S., Kossakowski, D., et al. 2020, *A&A*, 642, A236, doi: [10.1051/0004-6361/202038967](https://doi.org/10.1051/0004-6361/202038967)
- Kipping, D. M. 2013, *MNRAS*, 435, 2152, doi: [10.1093/mnras/stt1435](https://doi.org/10.1093/mnras/stt1435)
- Kollmeier, J. A., Rix, H.-W., Aerts, C., et al. 2026, *AJ*, 171, 52, doi: [10.3847/1538-3881/ae0576](https://doi.org/10.3847/1538-3881/ae0576)
- Kossakowski, D., Kemmer, J., Bluhm, P., et al. 2021, *A&A*, 656, A124, doi: [10.1051/0004-6361/202141587](https://doi.org/10.1051/0004-6361/202141587)
- Kovačević, T., González-Cataldo, F., Stewart, S. T., & Militzer, B. 2022, *NatSR*, 12, 13055, doi: [10.1038/s41598-022-16816-w](https://doi.org/10.1038/s41598-022-16816-w)
- Kumar, R., Carroll, C., Hartikainen, A., & Martin, O. A. 2019, *The Journal of Open Source Software*, doi: [10.21105/joss.01143](https://doi.org/10.21105/joss.01143)
- Kutra, T., Wu, Y., & Qian, Y. 2021, *AJ*, 162, 69, doi: [10.3847/1538-3881/ac0431](https://doi.org/10.3847/1538-3881/ac0431)
- Lafarga, M., Armstrong, D. J., Cui, K., et al. 2026, *MNRAS.tmp*, doi: [10.1093/mnras/stag512](https://doi.org/10.1093/mnras/stag512)
- Lagrange, A. M., Gratadour, D., Chauvin, G., et al. 2009, *A&A*, 493, L21, doi: [10.1051/0004-6361:200811325](https://doi.org/10.1051/0004-6361:200811325)
- Lee, E. J., & Chiang, E. 2015, *ApJ*, 811, 41, doi: [10.1088/0004-637X/811/1/41](https://doi.org/10.1088/0004-637X/811/1/41)
- Lee, E. J., Karalis, A., & Thorngren, D. P. 2022, *ApJ*, 941, 186, doi: [10.3847/1538-4357/ac9c66](https://doi.org/10.3847/1538-4357/ac9c66)
- Léger, A., Selsis, F., Sotin, C., et al. 2004, *Icar*, 169, 499, doi: [10.1016/j.icarus.2004.01.001](https://doi.org/10.1016/j.icarus.2004.01.001)

- Lightkurve Collaboration, Cardoso, J. V. d. M., Hedges, C., et al. 2018, Lightkurve: Kepler and TESS time series analysis in Python, *Astrophysics Source Code Library*. <http://ascl.net/1812.013>
- Lin, Z., & Seager, S. 2025, *ApJL*, 990, L35, doi: [10.3847/2041-8213/adfcc8](https://doi.org/10.3847/2041-8213/adfcc8)
- Lopez, E. D., & Rice, K. 2018, *MNRAS*, 479, 5303, doi: [10.1093/mnras/sty1707](https://doi.org/10.1093/mnras/sty1707)
- Lu, C. X., Schlafman, K. C., & Cheng, S. 2020, *AJ*, 160, 253, doi: [10.3847/1538-3881/abb773](https://doi.org/10.3847/1538-3881/abb773)
- Luger, R., Agol, E., Foreman-Mackey, D., et al. 2019, *AJ*, 157, 64, doi: [10.3847/1538-3881/aae8e5](https://doi.org/10.3847/1538-3881/aae8e5)
- Luque, R., & Pallé, E. 2022, *Sci*, 377, 1211, doi: [10.1126/science.abl7164](https://doi.org/10.1126/science.abl7164)
- Luque, R., Fulton, B. J., Kunimoto, M., et al. 2022a, *A&A*, 664, A199, doi: [10.1051/0004-6361/202243834](https://doi.org/10.1051/0004-6361/202243834)
- Luque, R., Nowak, G., Hirano, T., et al. 2022b, *A&A*, 666, A154, doi: [10.1051/0004-6361/202244426](https://doi.org/10.1051/0004-6361/202244426)
- MacDonald, M. G., Dawson, R. I., Morrison, S. J., Lee, E. J., & Khandelwal, A. 2020, *ApJ*, 891, 20, doi: [10.3847/1538-4357/ab6f04](https://doi.org/10.3847/1538-4357/ab6f04)
- MacDougall, M. G., Petigura, E. A., Gilbert, G. J., et al. 2023, *AJ*, 166, 33, doi: [10.3847/1538-3881/acd557](https://doi.org/10.3847/1538-3881/acd557)
- Maciejewski, G., Niedzielski, A., Nowak, G., et al. 2014, *AcA*, 64, 323, doi: [10.48550/arXiv.1501.02711](https://doi.org/10.48550/arXiv.1501.02711)
- Macintosh, B., Graham, J. R., Barman, T., et al. 2015, *Science*, 350, 64, doi: [10.1126/science.aac5891](https://doi.org/10.1126/science.aac5891)
- Majewski, S. R., Schiavon, R. P., Frinchaboy, P. M., et al. 2017, *AJ*, 154, 94, doi: [10.3847/1538-3881/aa784d](https://doi.org/10.3847/1538-3881/aa784d)
- Mallorquín, M., Goffo, E., Pallé, E., et al. 2023, *A&A*, 680, A76, doi: [10.1051/0004-6361/202347346](https://doi.org/10.1051/0004-6361/202347346)
- Mallorquín, M., Béjar, V. J. S., Lodieu, N., et al. 2024, *A&A*, 689, A132, doi: [10.1051/0004-6361/202450047](https://doi.org/10.1051/0004-6361/202450047)
- Mann, A. W., Brewer, J. M., Gaidos, E., Lépine, S., & Hilton, E. J. 2013a, *Astronomische Nachrichten*, 334, 18, doi: [10.1002/asna.201211758](https://doi.org/10.1002/asna.201211758)
- . 2013b, *AJ*, 145, 52, doi: [10.1088/0004-6256/145/2/52](https://doi.org/10.1088/0004-6256/145/2/52)
- Mann, A. W., Feiden, G. A., Gaidos, E., Boyajian, T., & von Braun, K. 2015, *ApJ*, 804, 64, doi: [10.1088/0004-637X/804/1/64](https://doi.org/10.1088/0004-637X/804/1/64)
- Mann, A. W., Gaidos, E., & Ansdell, M. 2013c, *ApJ*, 779, 188, doi: [10.1088/0004-637X/779/2/188](https://doi.org/10.1088/0004-637X/779/2/188)
- Mann, A. W., Gaidos, E., Kraus, A., & Hilton, E. J. 2013d, *ApJ*, 770, 43, doi: [10.1088/0004-637X/770/1/43](https://doi.org/10.1088/0004-637X/770/1/43)
- Mann, A. W., Dupuy, T., Muirhead, P. S., et al. 2017, *AJ*, 153, 267, doi: [10.3847/1538-3881/aa7140](https://doi.org/10.3847/1538-3881/aa7140)
- Mann, A. W., Dupuy, T., Kraus, A. L., et al. 2019, *ApJ*, 871, 63, doi: [10.3847/1538-4357/aaf3bc](https://doi.org/10.3847/1538-4357/aaf3bc)
- Mayo, A. W., Dressing, C. D., Vanderburg, A., et al. 2023, *AJ*, 165, 235, doi: [10.3847/1538-3881/acca1c](https://doi.org/10.3847/1538-3881/acca1c)
- Meier Valdés, E. A., Demory, B.-O., Diamond-Lowe, H., et al. 2025a, *A&A*, 698, A68, doi: [10.1051/0004-6361/202453449](https://doi.org/10.1051/0004-6361/202453449)
- . 2025b, *A&A*, 699, C1, doi: [10.1051/0004-6361/202556143e](https://doi.org/10.1051/0004-6361/202556143e)
- Ment, K., & Charbonneau, D. 2023, *AJ*, 165, 265, doi: [10.3847/1538-3881/acd175](https://doi.org/10.3847/1538-3881/acd175)
- Mistry, P., Prasad, A., Maity, M., et al. 2024, *PASA*, 41, e030, doi: [10.1017/pasa.2024.29](https://doi.org/10.1017/pasa.2024.29)
- Mordasini, C., Alibert, Y., Benz, W., Klahr, H., & Henning, T. 2012, *A&A*, 541, A97, doi: [10.1051/0004-6361/201117350](https://doi.org/10.1051/0004-6361/201117350)
- Mori, M., Livingston, J. H., Leon, J. d., et al. 2022, *AJ*, 163, 298, doi: [10.3847/1538-3881/ac6bf8](https://doi.org/10.3847/1538-3881/ac6bf8)
- Morton, T. D., Bryson, S. T., Coughlin, J. L., et al. 2016, *ApJ*, 822, 86, doi: [10.3847/0004-637X/822/2/86](https://doi.org/10.3847/0004-637X/822/2/86)
- Mousis, O., Deleuil, M., Aguichine, A., et al. 2020, *ApJL*, 896, L22, doi: [10.3847/2041-8213/ab9530](https://doi.org/10.3847/2041-8213/ab9530)
- Muñoz, J. L., & Evans, D. W. 2014, *Astronomische Nachrichten*, 335, 367, doi: [10.1002/asna.201312045](https://doi.org/10.1002/asna.201312045)
- Muirhead, P. S., Dressing, C. D., Mann, A. W., et al. 2018, *AJ*, 155, 180, doi: [10.3847/1538-3881/aab710](https://doi.org/10.3847/1538-3881/aab710)
- Mulders, G. D., Pascucci, I., Apai, D., Frasca, A., & Molenda-Żakowicz, J. 2016, *AJ*, 152, 187, doi: [10.3847/0004-6256/152/6/187](https://doi.org/10.3847/0004-6256/152/6/187)
- Ness, M., Hogg, D. W., Rix, H.-W., Ho, A. Y. Q., & Zasowski, G. 2015, *ApJ*, 808, 16, doi: [10.1088/0004-637X/808/1/16](https://doi.org/10.1088/0004-637X/808/1/16)
- Newton, E. R., Charbonneau, D., Irwin, J., et al. 2014, *AJ*, 147, 20, doi: [10.1088/0004-6256/147/1/20](https://doi.org/10.1088/0004-6256/147/1/20)
- . 2022, tellrv: Radial velocities for low-resolution NIR spectra, *Astrophysics Source Code Library*, record ascl:2201.007
- Ogihara, M., Morbidelli, A., & Guillot, T. 2015, *A&A*, 578, A36, doi: [10.1051/0004-6361/201525884](https://doi.org/10.1051/0004-6361/201525884)
- Önehag, A., Heiter, U., Gustafsson, B., et al. 2012, *A&A*, 542, A33, doi: [10.1051/0004-6361/201118101](https://doi.org/10.1051/0004-6361/201118101)
- Owen, J. E., & Murray-Clay, R. 2018a, *MNRAS*, 480, 2206, doi: [10.1093/mnras/sty1943](https://doi.org/10.1093/mnras/sty1943)
- . 2018b, *MNRAS*, 480, 2206, doi: [10.1093/mnras/sty1943](https://doi.org/10.1093/mnras/sty1943)
- Owen, J. E., & Wu, Y. 2013, *ApJ*, 775, 105, doi: [10.1088/0004-637X/775/2/105](https://doi.org/10.1088/0004-637X/775/2/105)
- Paegert, M., Stassun, K. G., Collins, K. A., et al. 2021, *arXiv*, arXiv:2108.04778, doi: [10.48550/arXiv.2108.04778](https://doi.org/10.48550/arXiv.2108.04778)
- . 2022, VizieR Online Data Catalog: TESS Input Catalog version 8.2 (TIC v8.2) (Paegert+, 2021), *VizieR On-line Data Catalog: IV/39*. Originally published in: 2021arXiv210804778P
- pandas development team, T. 2020, *pandas-dev/pandas: Pandas, latest*, Zenodo, doi: [10.5281/zenodo.3509134](https://doi.org/10.5281/zenodo.3509134)

- Parashivamurthy, H. M., & Mulders, G. D. 2025, *A&A*, 703, A8, doi: [10.1051/0004-6361/202554006](https://doi.org/10.1051/0004-6361/202554006)
- Parc, L., Bouchy, F., Venturini, J., Dorn, C., & Helled, R. 2024, *A&A*, 688, A59, doi: [10.1051/0004-6361/202449911](https://doi.org/10.1051/0004-6361/202449911)
- Pass, E. K., Cargile, P. A., DiTomasso, V., et al. 2025, *ApJS*, 281, 27, doi: [10.3847/1538-4365/ae0acb](https://doi.org/10.3847/1538-4365/ae0acb)
- Passegger, V. M., Bello-García, A., Ordieres-Meré, J., et al. 2022, *A&A*, 658, A194, doi: [10.1051/0004-6361/202141920](https://doi.org/10.1051/0004-6361/202141920)
- Peláez-Torres, A., Esparza-Borges, E., Pallé, E., et al. 2024, *A&A*, 690, A62, doi: [10.1051/0004-6361/202347251](https://doi.org/10.1051/0004-6361/202347251)
- Petigura, E. A. 2020, *AJ*, 160, 89, doi: [10.3847/1538-3881/ab9fff](https://doi.org/10.3847/1538-3881/ab9fff)
- Petigura, E. A., Marcy, G. W., Winn, J. N., et al. 2018, *AJ*, 155, 89, doi: [10.3847/1538-3881/aaa54c](https://doi.org/10.3847/1538-3881/aaa54c)
- Piaulet-Ghorayeb, C., Benneke, B., Radica, M., et al. 2024, *ApJL*, 974, L10, doi: [10.3847/2041-8213/ad6f00](https://doi.org/10.3847/2041-8213/ad6f00)
- Poultourtzidis, E., Lacedelli, G., Pallé, E., et al. 2026, *A&A*, 707, A106, doi: [10.1051/0004-6361/202557155](https://doi.org/10.1051/0004-6361/202557155)
- Quintana, E. V., Barclay, T., Raymond, S. N., et al. 2014, *Sci*, 344, 277, doi: [10.1126/science.1249403](https://doi.org/10.1126/science.1249403)
- Rajpurohit, A. S., Allard, F., Rajpurohit, S., et al. 2018, *A&A*, 620, A180, doi: [10.1051/0004-6361/201833500](https://doi.org/10.1051/0004-6361/201833500)
- Rayner, J. T., Onaka, P. M., Cushing, M. C., & Vacca, W. D. 2004, in *Society of Photo-Optical Instrumentation Engineers (SPIE) Conference Series*, Vol. 5492, *Ground-based Instrumentation for Astronomy*, ed. A. F. M. Moorwood & M. Iye, 1498–1509, doi: [10.1117/12.551107](https://doi.org/10.1117/12.551107)
- Rayner, J. T., Toomey, D. W., Onaka, P. M., et al. 2003a, *PASP*, 115, 362, doi: [10.1086/367745](https://doi.org/10.1086/367745)
- . 2003b, *PASP*, 115, 362, doi: [10.1086/367745](https://doi.org/10.1086/367745)
- Reefe, M. A., Luque, R., Gaidos, E., et al. 2022, *AJ*, 163, 269, doi: [10.3847/1538-3881/ac658b](https://doi.org/10.3847/1538-3881/ac658b)
- Ribas, Á., Bouy, H., & Merín, B. 2015, *A&A*, 576, A52, doi: [10.1051/0004-6361/201424846](https://doi.org/10.1051/0004-6361/201424846)
- Ricker, G. R., Winn, J. N., Vanderspek, R., et al. 2015, *JATIS*, 1, 014003, doi: [10.1117/1.JATIS.1.1.014003](https://doi.org/10.1117/1.JATIS.1.1.014003)
- Rodriguez, J. E., Becker, J. C., Eastman, J. D., et al. 2018, *AJ*, 156, 245, doi: [10.3847/1538-3881/aae530](https://doi.org/10.3847/1538-3881/aae530)
- Rogers, J. G., Dorn, C., Aditya Raj, V., Schlichting, H. E., & Young, E. D. 2025, *ApJ*, 979, 79, doi: [10.3847/1538-4357/ad9f61](https://doi.org/10.3847/1538-4357/ad9f61)
- Rogers, L. A. 2015, *ApJ*, 801, 41, doi: [10.1088/0004-637X/801/1/41](https://doi.org/10.1088/0004-637X/801/1/41)
- Rosenblatt, F. 1971, *Icar*, 14, 71, doi: [10.1016/0019-1035\(71\)90103-5](https://doi.org/10.1016/0019-1035(71)90103-5)
- Salvatier, J., Wiecki, T. V., & Fonnesbeck, C. 2016, *PeerJ Computer Science*, 2, e55
- Sandoval, A., Cañas, C. I., Kanodia, S., et al. 2026, *AJ*, 171, 43, doi: [10.3847/1538-3881/ae16a2](https://doi.org/10.3847/1538-3881/ae16a2)
- Santos, N. C., Israelian, G., & Mayor, M. 2001, *A&A*, 373, 1019, doi: [10.1051/0004-6361:20010648](https://doi.org/10.1051/0004-6361:20010648)
- Sarkis, P., Henning, T., Kürster, M., et al. 2018, *AJ*, 155, 257, doi: [10.3847/1538-3881/aac108](https://doi.org/10.3847/1538-3881/aac108)
- Schlaufman, K. C. 2018, *ApJ*, 853, 37, doi: [10.3847/1538-4357/aa961c](https://doi.org/10.3847/1538-4357/aa961c)
- Schlecker, M., Pham, D., Burn, R., et al. 2021, *A&A*, 656, A73, doi: [10.1051/0004-6361/202140551](https://doi.org/10.1051/0004-6361/202140551)
- Schlieder, J. E., Crossfield, I. J. M., Petigura, E. A., et al. 2016, *ApJ*, 818, 87, doi: [10.3847/0004-637X/818/1/87](https://doi.org/10.3847/0004-637X/818/1/87)
- Scholz, F. W., & Stephens, M. A. 1987, *Journal of the American Statistical Association*, 82, 918. <http://www.jstor.org/stable/2288805>
- Silverstein, M. L., Schlieder, J. E., Barclay, T., et al. 2022, *AJ*, 163, 151, doi: [10.3847/1538-3881/ac32e3](https://doi.org/10.3847/1538-3881/ac32e3)
- Silverstein, M. L., Barclay, T., Schlieder, J. E., et al. 2024, *AJ*, 167, 255, doi: [10.3847/1538-3881/ad3040](https://doi.org/10.3847/1538-3881/ad3040)
- Soubkiou, A., Barkaoui, K., Benkhaldoun, Z., et al. 2025, *MNRAS*, 541, 3249, doi: [10.1093/mnras/staf1030](https://doi.org/10.1093/mnras/staf1030)
- Stassun, K. G., Oelkers, R. J., Pepper, J., et al. 2018, *AJ*, 156, 102, doi: [10.3847/1538-3881/aad050](https://doi.org/10.3847/1538-3881/aad050)
- Stassun, K. G., Oelkers, R. J., Paegert, M., et al. 2019, *AJ*, 158, 138, doi: [10.3847/1538-3881/ab3467](https://doi.org/10.3847/1538-3881/ab3467)
- Stefansson, G., Mahadevan, S., Maney, M., et al. 2020, *AJ*, 160, 192, doi: [10.3847/1538-3881/abb13a](https://doi.org/10.3847/1538-3881/abb13a)
- TESS Team. 2018, *TESS Input Catalog and Candidate Target List*, STScI/MAST, doi: [10.17909/FWDT-2X66](https://doi.org/10.17909/FWDT-2X66)
- Theano Development Team. 2016, *arXiv e-prints*, [abs/1605.02688](https://arxiv.org/abs/1605.02688). <http://arxiv.org/abs/1605.02688>
- Tingley, B. 2004, *A&A*, 425, 1125, doi: [10.1051/0004-6361:20035792](https://doi.org/10.1051/0004-6361:20035792)
- Torres, G., Kipping, D. M., Fressin, F., et al. 2015, *ApJ*, 800, 99, doi: [10.1088/0004-637X/800/2/99](https://doi.org/10.1088/0004-637X/800/2/99)
- Torres, G., Kane, S. R., Rowe, J. F., et al. 2017, *AJ*, 154, 264, doi: [10.3847/1538-3881/aa984b](https://doi.org/10.3847/1538-3881/aa984b)
- Trifonov, T., Caballero, J. A., Morales, J. C., et al. 2021, *Sci*, 371, 1038, doi: [10.1126/science.abd7645](https://doi.org/10.1126/science.abd7645)
- Tull, R. G., MacQueen, P. J., Sneden, C., & Lambert, D. L. 1995, *PASP*, 107, 251, doi: [10.1086/133548](https://doi.org/10.1086/133548)
- Vacca, W. D., Cushing, M. C., & Rayner, J. T. 2003, *PASP*, 115, 389, doi: [10.1086/346193](https://doi.org/10.1086/346193)
- Van Eylen, V., Astudillo-Defru, N., Bonfils, X., et al. 2021, *MNRAS*, 507, 2154, doi: [10.1093/mnras/stab2143](https://doi.org/10.1093/mnras/stab2143)
- Venturini, J., Guilera, O. M., Haldemann, J., Ronco, M. P., & Mordasini, C. 2020, *A&A*, 643, L1, doi: [10.1051/0004-6361/202039141](https://doi.org/10.1051/0004-6361/202039141)
- Venturini, J., Ronco, M. P., Guilera, O. M., et al. 2024, *A&A*, 686, L9, doi: [10.1051/0004-6361/202349088](https://doi.org/10.1051/0004-6361/202349088)

- Wanderley, F., Cunha, K., Souto, D., Smith, V. V., & Daflon, S. 2025, *AJ*, 170, 177, doi: [10.3847/1538-3881/ade1f2](https://doi.org/10.3847/1538-3881/ade1f2)
- Wang, J., & Fischer, D. A. 2015, *AJ*, 149, 14, doi: [10.1088/0004-6256/149/1/14](https://doi.org/10.1088/0004-6256/149/1/14)
- Wells, R., Poppenhaeger, K., & Watson, C. A. 2019, *MNRAS*, 487, 1865, doi: [10.1093/mnras/stz1334](https://doi.org/10.1093/mnras/stz1334)
- Wes McKinney. 2010, in *Proceedings of the 9th Python in Science Conference*, ed. Stéfan van der Walt & Jarrod Millman, 56 – 61, doi: [10.25080/Majora-92bf1922-00a](https://doi.org/10.25080/Majora-92bf1922-00a)
- Williams, J. P., & Cieza, L. A. 2011, *ARA&A*, 49, 67, doi: [10.1146/annurev-astro-081710-102548](https://doi.org/10.1146/annurev-astro-081710-102548)
- Wilson, J. C., Hearty, F. R., Skrutskie, M. F., et al. 2019, *PASP*, 131, 055001, doi: [10.1088/1538-3873/ab0075](https://doi.org/10.1088/1538-3873/ab0075)
- Xenos, K. O., Bitsch, B., & Andama, G. 2025, *A&A*, 701, A47, doi: [10.1051/0004-6361/202555591](https://doi.org/10.1051/0004-6361/202555591)